9

Designing super-lenses

The previous chapter focused on the essential ideas of the *Perfect Lens*. The perfect lens is an ideal imaging device that requires ideal materials with $\varepsilon = \mu = -1$ for image resolution without limit. It was shown that very small deviations of the material parameters from these ideal conditions could lead to the excitation of resonances that cause deterioration of the performance of the lens. In addition, finite amounts of dissipation and other imperfections that occur in actual materials have been shown to also limit the resolution of this device. Substantial subwavelength resolution is, however, possible in spite of dissipation, and the lenses exhibiting some degree of subwavelength image resolution capabilities have been termed *Super-Lenses*.

It turns out that the Veselago lens is only one of a whole class of perfect lenses or super-lenses that are possible. Negative refractive media (NRM) with ($\varepsilon < 0$, $\mu < 0$) are the optical analogue of anti-matter, in the sense that the effects on radiation (amplitude and phase change) upon passage through negative refractive index media nullifies the effects (amplitude and phase change) of passing through an equal thickness of positive media with the same magnitudes of ε and μ (Pendry and Ramakrishna 2003). This concept of complementarity has lead to the generalization of the Veselago lens to slab pairs of complementary optical media (Pendry and Ramakrishna 2003) as well as to other geometries via a geometric transformation technique (Ward and Pendry 1996). One can also achieve magnification of the near-field images in the cylindrical (Pendry and Ramakrishna 2002, Pendry 2003) and spherical (Ramakrishna and Pendry 2004) geometries. In addition, super-lens behavior is also exhibited in structures involving sharp corners and wedges of negative refractive index media.

Another interesting class of imaging devices are based on anisotropic media where some components of the material tensors such as $\bar{\bar{\varepsilon}}$ and $\bar{\bar{\mu}}$ are negative while others are positive – the so-called *indefinite media* (see Section 5.3.1). Waves that are evanescent in ordinary media would become propagating inside such media due to the hyperbolic nature of their dispersion. Thus one can project out the evanescent waves from a source across large thicknesses of these media and even outcouple the near-field information to the far-field. Such a super-lens has been called a *Hyperlens* (Jacob et al. 2006), after the hyperbolic nature of the dispersion that makes its functioning possible. The hyperlens, which outcouples to the far field, has enormous potential applications in near-field imaging and has already been demonstrated experimentally (Liu et al.

2007).

In this chapter, we discuss a variety of super-lenses with different geometries, and with an intention to reduce the deteriorating effects of dissipation and imperfections in the materials used in the construction of such super-lenses. We note that any deviations from the ideal conditions for perfect lensing leads to a drastic reduction in the possible subwavelength resolution of the super-lens. In fact, it is absorption that is the main culprit responsible for reducing the resolution. In the case of the silver lens, one merely manages to obtain some subwavelength image information. Minimizing the effects of absorption is therefore crucial in order to make these imaging devices work. Restructuring the lens to reduce these effects is possible to some extent and we first discuss some such strategies. Eventually it does, however, appear that the composite structures would need to incorporate media with active gain (as in a laser) in order to counter dissipation (Tretyakov 2001, Ramakrishna and Pendry 2003, Pendry and Smith 2004).

9.1 Overcoming the limitations of real materials

Real materials with negative real parts of ε and μ pose several challenges for the implementation of super-lenses. Of course, it is imperative to ensure that the materials practically have excellent chemical composition and smooth surfaces, so that the metamaterials have as few imperfections as possible, and also meet the perfect lens conditions for the real parts of the material parameters as accurately as possible at the operating frequency. In particular, the main restriction for obtaining high levels of image resolution with most metamaterials or metals is the presence of large levels of dissipation. Given the fact that materials with negative material parameters usually depend on a resonance for their property, there is necessarily at least some level of absorption near the resonance.* Hence if the level of absorption in the metamaterial cannot itself be reduced, the principal task at hand is to see how to reduce the effects of absorption that degrade the image quality. Potentially a different geometry or frequency could enhance the image resolution. For example, in Section 8.2.3, we could increase the resolution of the slab lens just by choosing the asymmetric configuration with a large dielectric constant on the far side of the slab. It has also been shown that in the asymmetric lens, one could obtain a better image resolution at a slightly lower frequency than when $\varepsilon_2 = -\varepsilon_3$ because then the frequency $\omega = \omega_p/\sqrt{1+\varepsilon_3}$ comes into

*The Kramers-Kronig (see Eqs. (1.9)) relations which relate the real and imaginary parts of the material parameters impose that the imaginary part would be large at frequencies near the resonance where the real part disperses violently and can be negative.

better overlap with the resonant excitations of the surface plasmon dispersion curve at larger transverse wave-vectors (Ramakrishna et al. 2002).

9.1.1 Layering the lens

One possibility to reduce the effects of absorption is to decrease the slab thickness since the evanescent fields amplify in magnitude to much smaller levels in thinner slabs. As absorption is maximal in regions of large electromagnetic fields, the total absorption immediately reduces as a consequence of smaller electromagnetic fields. Larger wave-vectors can then contribute to the image thereby enhancing the image resolution. Note that it is the ratio λ/d (wavelength to slab thickness) that dominates the resolution, the logarithm term being a relatively weakly varying function (see Eq. (8.24)). For example, if $\lambda/d = 3$, we find that $\delta\varepsilon$ must be no greater than about $\sim 10^{-11}$ to achieve a resolution factor of 10. Comparatively, $\delta\varepsilon$ can be as large as ~ 0.002 for $\lambda/d = 10$ while still achieving the same resolution. In this case, however, the actual distance over which the image is transferred becomes smaller. Hence just making the slab thinner is not a satisfactory solution in most cases.

With ideal lossless negative index media satisfying the perfect lens conditions, we could just take the original thick slab, divide it into thin layers, and redistribute the layers alternatively between the source and the image planes without affecting the result of perfect imaging thanks to the perfect impedance matching (Shamonina et al. 2001, Ramakrishna et al. 2003). The evanescent fields alternatively grow within the NRM layers and decay in the positive layers as shown in Fig. 9.1. This rearrangement, however, makes an enormous difference to the dissipation in the system. As the fields do not amplify to the same extent as they would have to in the single slab, the associated dissipation is significantly decreased. However, we note that the (object plane – lens-edge) and the (lens-edge – image plane) distances have reduced considerably. In the limit of very small layer thicknesses, these distances become extremely small and the layered system merely transfers the image of the source from one edge to the other in the manner of an optical fiber bundle. Note, however, that the image transfer here involves both the near-field and the radiative modes.

While the idea of layering the lens is straightforward for negative index media, it is not absolutely clear if this configuration works in the case of the silver lens (see Section 8.2.2) where there is a finite impedance mismatch at the boundaries. Admittedly in the limit of small lengthscales (quasi-static limit), the near-field solutions for the silver lens should appear to be similar to the negative index medium. In Fig. 9.2, the transfer function for the intensity from the object plane to the image plane for P-polarized light has been plotted as a function of the parallel component of the wave-vector. Since only the relative material parameters are relevant for the single frequency problem, we assume without loss of generality that the positive medium has $\varepsilon_+ = 1$ and $\mu_+ = 1$. In the case of a hypothetical negative dielectric medium with no

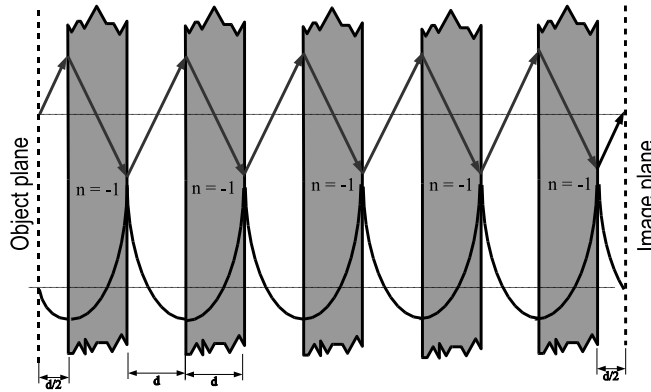

Figure 9.1 Chopping the slab of NRM into thin slices and distributing them around does not affect the image. The field distributions for a system of five such pieces is depicted schematically. The evanescent fields amplify along the direction normal to the layers ($\hat{z}$) within the negative index slabs and decay exponentially along $\hat{z}$ in the normal media. The rays corresponding to the propagating waves that undergo negative refraction at each interface and come to a focus at the image plane.

losses ($\varepsilon_- = -1$, $\mu = +1$), we see that the transmittance is nearly unity for a significant interval of the subwavelength wave-vectors and is dominated by the presence of a series of resonances at subwavelength wave-vectors. These are due to the hybridized resonances of the layered stack that arise from the coupling of the surface plasmons on the individual interfaces. In the limit of a periodic layered medium, these would give rise to continuous bands for the surface plasmons in the system. Because the individual layer thickness is very small, these coupled excitations have large wave-vectors for $\omega = \omega_p/\sqrt{2}$ as they are detuned only slightly from the surface plasmon frequency of the semi-infinite negative medium. The cutoff wave-vector is large for the imaging process and only depends on the thickness of the individual layers. The cutoff wave-vector is given by the value of k_x for the intersection between the $\omega = \omega_p/\sqrt{2}$ line and the most detuned asymmetric stack plasmon branch. This turns out to be slightly larger than the limit given in Section 8.3 for a given thickness of the individual negative dielectric layers with $\mu = 1$. Thus, the idea of layering up the silver lens gets us closer to the electrostatic limit where μ becomes irrelevant for the P-polarized light. In the presence of dissipation, however, these modes are damped and the resonances broaden out. Absorption causes deterioration of the image resolution and then the layered stack yields an image resolution far worse than the limit set by retardation for the individual thin layers (see Eq. (8.27)). Nonetheless, the transfer function shows that much higher image resolution can be obtained by using such a

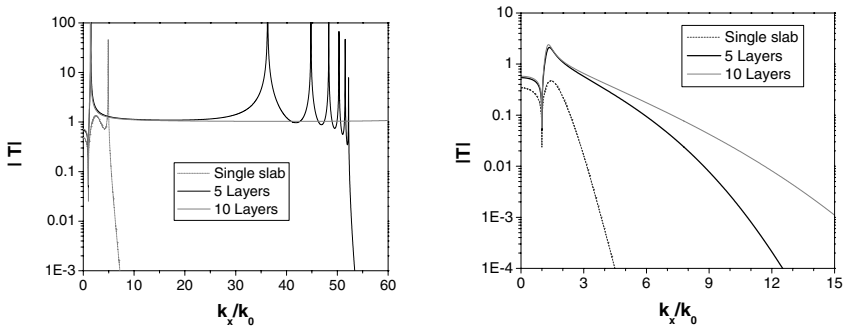

Figure 9.2 Modulus of the transmitted fields for P-polarized light at the image plane for a stack of alternating equally thick layers of a negative dielectric medium (silver) and a positive dielectric medium of equal thickness. The total distance from the object plane to the image plane is 100 nm. The other distances are (i) for a single slab of silver, layer thickness = 50 nm; (ii) for 5 layers of silver in-between, the layer thickness is 10 nm; and (iii) for 10 layers of silver in-between, the layer thickness is 5 nm. Left: The fields at the image plane for hypothetical lossless negative medium with $\varepsilon = -1$. Right: The fields at the image plane for silver layers with $\varepsilon = -1 + \mathrm{i}0.4$. The positive media are assumed to have $\varepsilon = +1$ in both cases. The wavelength assumed is 358 nm about where $\mathrm{Re}(\varepsilon) = -1$ for silver.

layered stack than the single slab lens in spite of dissipation in the medium. Experiments have indicated that while the image resolution is better for a double layer than for a single layer lens, the image fidelity suffers due to enhanced surface roughness in the experimental implementation of the bi-layer lens (Melville and Blaikie 2006). Clearly, surface roughness and evenness of the layers become important technological issues that need to be resolved for the multilayer lens.

9.1.2 A layered stack to direct radiation

When the thickness δ of the individual layers becomes very small compared to the wavelength, it is fruitful to think of the layered stack as a slab of effective medium (Fig. 9.3). The effective response of a layered medium has been considered in Section 2.5 and has been shown to be anisotropic. For the response of a layered stack of a medium with equal layer thickness of the negative permittivity medium and the positive medium, one obtains

$$\varepsilon_x = \frac{(\varepsilon_+ + \varepsilon_-)}{2}, \tag{9.1}$$

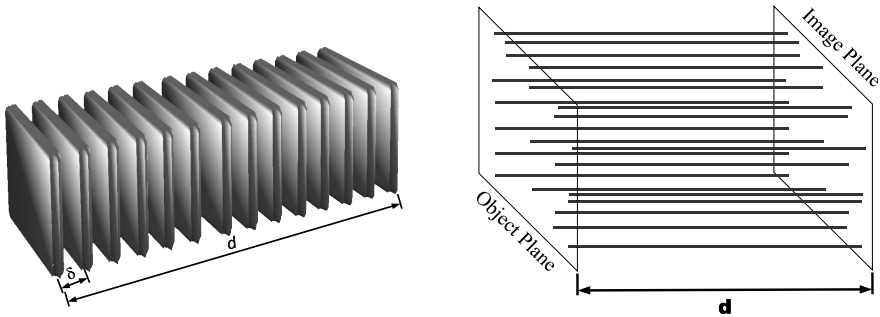

Figure 9.3 Left: Layered medium consisting of alternately negative and positive dielectric layers of equal thickness $\delta/2$. The layered stack behaves as a slab of an effective medium in the limit of very small layer thickness. Right: The picture schematically depicts how the anisotropic medium is equivalent to the electrostatic case of the two ends of the slab being connected point by point with perfectly conducting wires going through an insulating medium.

if the electric field is applied parallel to the layers and the tangential component of the **E** field is continuous across the layer boundaries. Similarly, considering the response to an electric field applied normal to the layers, we obtain

$$\varepsilon_z = \frac{2}{(\varepsilon_+^{-1} + \varepsilon_-^{-1})}, \tag{9.2}$$

where the continuity of the normal component of the **D** field is implied. Under the perfect lens conditions, we have the effective medium dielectric permittivity components

$$\varepsilon_x \to 0, \qquad \varepsilon_z \to \infty, \tag{9.3}$$

and the layered stack acts as a slab of an unusual anisotropic medium. Similar relations can be derived for the magnetic permeability using the continuity of $\mathbf{H}_{\|}$ and $\mathbf{B}_{\perp}$.

The wave propagation for the P-polarized radiation in such an uniaxially anisotropic medium has the dispersion similar to the S-polarization given by Eq. (5.6),

$$\frac{k_x^2}{\varepsilon_z} + \frac{k_z^2}{\varepsilon_x} = \mu_y \frac{\omega^2}{c^2}, \tag{9.4}$$

where we assume $k_y = 0$ without loss of generality. In the limit of the perfect lens conditions, $\varepsilon_x \to 0$ and $\varepsilon_z \to \infty$, we have $k_z = 0$ as the only solution to the dispersion equation. Thus, every wave passes through this anisotropic material slab without any change in amplitude or phase (Ramakrishna et al. 2003). In the static limit and no dissipation, the situation corresponds to infinitely thin and perfectly conducting wires embedded in an insulating medium with $\varepsilon = 0$, and running down the slab connecting the two end-faces of the slab

of the effective medium point to point as depicted schematically in Fig. 9.3. Thus, the potential on one face is just directly transferred onto the other face and the layered stack acts as an optical fiber bundle, although it also transmits the near-field information (unlike a conventional optical fiber bundle). When there is dissipation, the wires acquire a finite thickness and consequently give a finite image resolution.

Having shown that the layered stack is equivalent to a slab of an unusual anisotropic effective medium, we now investigate the robustness against dissipation of the image resolution obtained by this slab. Since the dissipation mainly comes in via the negative dielectric medium, we consider the case $\varepsilon_- = -\varepsilon_+ + \mathrm{i}\delta\epsilon$ for the negative dielectric layers. Hence we have the different components of the effective permittivity as $\varepsilon_x = \mathrm{i}\ \delta\epsilon/2$ and $\varepsilon_z = -2\mathrm{i}\varepsilon_+(-\varepsilon_+ + \mathrm{i}\ \delta\epsilon)/(\delta\epsilon)$. The transmission coefficient for P-polarized light across the anisotropic slab of thickness d is given by (see Appendix B for a more general bianisotropic case)

$$T_p = \frac{1}{\cos(k_{z2}d) - \frac{\mathrm{i}}{2}(K + \frac{1}{K})\sin(k_{z2}d)}, \tag{9.5}$$

where $K = k_{z2}/(\varepsilon_x k_{z1})$, k_{z2} is the wave-vector in the slab, and k_{z1} is the wave-vector in the medium (with ε_+) outside the slab. Substituting for the wave-vectors in the quasi-static limit of $\omega \to 0$ or $k_x \to \infty$, we obtain $k_{z1} \to \mathrm{i}k_x$, $k_{z2} \to \mathrm{i}(\delta\epsilon)/(2\varepsilon_+)\ k_x$, and $K = 1/(\mathrm{i}\varepsilon_+)$. Hence the transmission coefficient in this limit becomes (Ramakrishna et al. 2003)

$$T_p = \left[\cosh(\frac{\delta\epsilon}{2\varepsilon_+}d) + \frac{\mathrm{i}}{2}\left(\varepsilon_+ - \frac{1}{\varepsilon_+}\right)\sinh(\frac{\delta\epsilon}{2\varepsilon_+}d)\right]^{-1}. \tag{9.6}$$

For the case when $\varepsilon_+ = 1$ as for vacuum, we have $T_p = \mathrm{sech}(\delta\epsilon\ k_x d/2)$. It is easy to see that the transmittance is of the order of unity for $\delta\epsilon\ k_x d \sim 1$, and hence that the resolution only depends inversely on the dissipation in the medium

$$\mathrm{res} = \frac{\lambda}{2\pi\ d\ \delta\epsilon}. \tag{9.7}$$

This should be compared to the slowly varying logarithmic dependence on the dissipation in the case of the single negative refractive index slab Eq. (8.25). The scope for improvement in the image resolution by making the metamaterials less dissipative is much higher in this case of the anisotropic layered medium. One should note that Wiltshire et al. (2003b) have experimentally obtained a similar imaging for S-polarized radio frequency waves at about 21 MHz using Swiss roll cylindrical metamaterials with the cylinders aligned along the imaging axis, which give a large value of μ_z near the resonance frequency and $\mu_x = 1$. It was found that the resolution is limited to 10 mm, approximately equal to the diameter of the individual Swiss rolls.

Actually the wave dispersion in such anisotropic media can be utilized much more creatively. *Indefinite* media with different signs for the components of

the material parameter tensors were discussed in Section 5.3.1 and it was shown that negative refraction is possible at the interface of such media. It was pointed out in (Smith and Schurig 2003) that the hyperbolic nature of the dispersion in certain indefinite media could imply that evanescent waves in vacuum could become propagating inside these media. As an example, let us rewrite the dispersion for the z-component of the wave-vector for P-polarized waves given by Eq. (9.4) as

$$k_z^2 = \varepsilon_x \mu_y \frac{\omega^2}{c^2} - \frac{\varepsilon_x}{\varepsilon_z} k_x^2, \tag{9.8}$$

where k_x is determined by the incident radiation. It is immediately clear that if $\varepsilon_x \mu_y > 0$ and $\varepsilon_x/\varepsilon_z < 0$, there are no evanescent waves in this medium (x-hyperbolic dispersion of Section 5.3.1). It was shown how to obtain an indefinite anisotropic medium by using alternating layers of a metal and dielectric with suitable volume fractions in Section 2.5. A look at Fig. 2.5 reveals that while $\mu_y = 1$, $\varepsilon_x < 0$, and $\varepsilon_z > 0$ at smaller frequencies in such media. In such a metamaterial, there is a cutoff wave-vector below which the waves in the effective medium are evanescent and above which waves are propagating (z-hyperbolic dispersion of Section 5.3.1). Incident evanescent waves with large parallel component of the wave-vector would couple to propagating modes in this medium. In the quasi-static limit, one can write

$$k_z = \pm \sqrt{\frac{-\varepsilon_x}{\varepsilon_z}} k_x. \tag{9.9}$$

The waves with large k_x have almost a specific direction of propagation in the anisotropic medium along the angle $\theta = \pm \tan^{-1}(\sqrt{\varepsilon_z/\varepsilon_x})$ to the $\hat{z}$-axis, which is the directional property of the anisotropic medium.

Theoretical studies on such slabs have been reported (Wood et al. 2006) where it has been shown that the location of the image moves outward in the transverse direction due to this preferred direction of propagation for large k_x, and can also get periodically repeated due to multiple reflections in the slab. Very good subwavelength image resolution of about $\lambda/10$ was shown to be obtainable with thin layers of silver (about few nanometers thick) and in spite of the large levels of dissipation in silver ($\mathrm{Im}(\varepsilon) \sim 0.4$). Resonant modes corresponding to the slab resonances of the anisotropic slab were excited by incident evanescent waves and measured in experiments (Wiltshire et al. 2003b) with Swiss-roll slabs of $\mu_z < 0$, $\mu_x = 1$. The resonances essentially occurred at values of $k_x d/\sqrt{\mu_z} = m\pi$ where m is an integer and d is the thickness of the slab. Of course, there would be a cutoff limit on the largest k_x that can be transported in this manner. This would either again be limited by spatial lengthscales of the underlying metamaterial units. It has pointed out in Wood et al. (2006) that for a periodic layered medium with period δ, a bandgap would essentially develop once the k_z in the medium became large enough, i.e., of the order $2\pi/\delta$ which sets a cutoff for the parallel wave-vector

as there would not be any propagating modes for larger wave-vectors at the given frequency. Indefinite media represent an interesting opportunity for subwavelength imaging as they are not as susceptible to dissipation since the electromagnetic fields have been distributed around more uniformly in space in comparison to the perfect lens.

9.1.3 Use of amplifying media to reduce dissipation

Although the image resolution of the layered lens is less susceptible to dissipation, the latter still plays a fundamental role in defining the performance of all the imaging devices. Since most metamaterials have appreciable levels of dissipation, we need to consider whether there is some way by which the energy lost by absorption can be reintroduced into the system. One intuitive idea would be to use optical amplification for this purpose (Ramakrishna and Pendry 2003).

Let us note that the dissipation in materials with negative material parameters actually represents a mismatch in the perfect lens conditions. One way to view it would be to regard the perfect lens conditions as conditions on the complex material parameters:

$$\varepsilon_+ = \varepsilon'_+ - \mathrm{i}\varepsilon''_+, \qquad \varepsilon_- = -\varepsilon'_+ + \mathrm{i}\varepsilon''_+, \tag{9.10a}$$

$$\mu_+ = \mu'_+ - \mathrm{i}\mu''_+, \qquad \mu_- = -\mu'_+ + \mathrm{i}\mu''_+, \tag{9.10b}$$

where the quantities $\mu''_+ \geq 0$ and $\varepsilon''_+ \geq 0$. We note that $\mathrm{Im}(\varepsilon_+) < 0$ and $\mathrm{Im}(\mu_+) < 0$ correspond to amplifying media. Consequently, the use of amplifying media to counter absorption using stimulated emission is implied in the perfect lens conditions itself.

In principle, surface plasmon excitations can be sustained across such an interface of a positive and amplifying medium with a negative and absorbing medium and have an interesting aspect to them: there is a continuous flow of electromagnetic energy from the amplifying medium into the absorbing medium that serves as a sink for the energy. Reduction in the damping for the surface plasmons propagating on the interface of silver and a laser pumped organic dye (Rhodamine 101 or Cresyl violet) solution has been reported (Seidel et al. 2005). The actual reason that amplification can compensate for the loss of information via absorption is because both absorption and stimulated emission are coherent processes. In the limit of large intensities (photon numbers), operation by the (quantum) annihilation operator does not alter the phase of a coherent photon state. There is, of course, some generation of noise via the spontaneous emission, which is an expression of the non-commutativity of the creation and annihilation operators. But as long as the amplification does not lead to self-sustaining oscillations of some modes in the lens structure, the amplification in one region can compensate for the absorption in another region of space. If self-sustaining oscillations occur, however, one is only amplifying the spontaneously generated photons, which swamp out all

the image information. The amplification levels are also likely to get saturated in the presence of intense field enhancements that are expected in the presence of surface plasmon resonances. The largest field enhancements occurs for the largest transverse wave-vectors. If we make the layers very thin, the local field enhancements are not as intense and it is likely that the gain will not get completely bleached.

More realistically, we can have optical amplification primarily for the electric dipole transitions. The incorporation of gain through the magnetic permeability would necessarily be through electronic amplifiers in the metamaterials for the microwave and radio frequencies. Let us consider here the case of alternating thin layers of silver with positive amplifying dielectric media layers of the same thickness in-between. Since only thin layers are being considered, we shall concentrate on the P-polarized light for which the negative dielectric permittivity is sufficient to make a super-lens in the quasi-static limit. Note that $\mu = 1$ in all such cases and the requirements for resonant surface plasmon excitations are met only in the quasi-static limit. Hence the incorporation of positive media with gain would be mainly for the situations where the quasi-static approximation works well, for example, in the layered lens rather the single slab lens. An implementation could be to use a semiconductor laser material such as GaN or AlGaAs for the positive medium and silver for the negative medium. Using blue/ultraviolet (UV) light to pump the AlGaAs,[†] one can make the AlGaAs optically amplifying in the red region of the spectrum, where one can satisfy the perfect lens condition for the real parts of the dielectric permittivity. Alternatively one could also use other high gain processes such as Raman gain for this purpose.

As a proof of principle, the transmission function for the layered silver lens, with and without amplification to exactly compensate for the losses, and the images of two closely spaced sources as resolved by the respective lenses is shown in Fig. 9.4. For comparison, we also show the case of the original single slab of silver as the lens (solid line and $\delta/2 = 40$ nm) and a layered, but gain-less system. The two peaks in the image for the single slab can hardly be resolved, while they are clearly resolved in the case of the layered system with no gain. The improvement in the image resolution for the layered system with gain over the corresponding gain-less systems is obvious with the sharp edges of the slits becoming visible. The transmittance of the layered lens with gain does not decay rapidly with the increase in the number of layers, even when the total stack thickness is about a few wavelengths (Ramakrishna and Pendry 2003). Although the transmission function is not constant with the wave-vector due to the excitation of the layer plasmon resonances, it should be emphasized that the high spatial frequency components are efficiently transferred across. Knowledge of the transfer function of the lens would therefore enable one to computationally recover a clean image from the observed image.

[†]The layers of silver will be transparent to UV radiation.

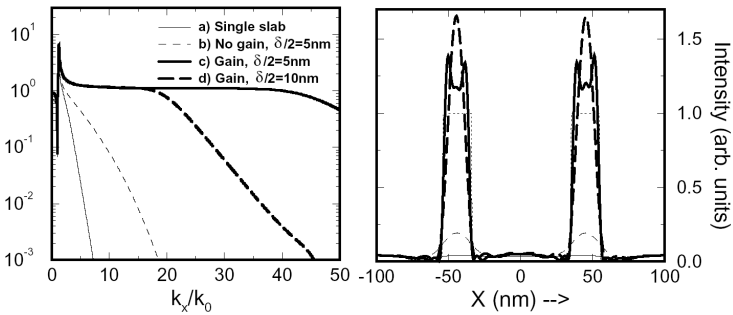

Figure 9.4 Transmission function (left) and electromagnetic field intensity at the image plane (right) obtained (a) with a single slab of silver of 40 nm thickness; (b) when the slab is split into 8 thin layers of $\delta/2 = 5$ nm thicknesses; (c) layered silver-dielectric stack with optical gain and $\delta/2 = 5$ nm and (d) layered silver-dielectric stack with optical gain and $\delta/2 = 10$ nm. $\varepsilon_{\pm} = \pm 1 \mp \mathrm{i}0.4$ in (c) and (d). (Reproduced with permission from Ramakrishna (2005). © 2005, Institute of Physics Publishing, U.K.)

The levels of gain to exactly compensate for the absorption in the metal are extremely large, and perhaps can just be achieved in some very high gain physical systems. But the incorporation of even some lower levels of gain in the positive parts of the lens will certainly lead to some enhancement of the image resolution. With the single slab super-lens, the enhancement in image resolution due to incomplete compensation of absorption can be marginal as the resolution depends logarithmically on the deviations from the perfect lens conditions. Nevertheless, for the layered lens with very thin layers and the lenses based on indefinite media where the image resolution depends inversely on the dissipation, even a partial compensation of the absorption by gain can lead to large improvements in the image resolution.

9.2 Generalized perfect lens theorem

The perfect slab lens as well as the layered lenses that we have previously described have a translational invariance along the transverse directions. It is this translational invariance that ensures that the image is identical in size to the source. In the case of the finite transverse lens, we broke the translational invariance and found that cavity-like effects can become important. We therefore ask ourselves whether the translation invariance in the transverse directions is essential to the functioning of the lens. It turns out that the translational invariance can be broken, the material parameters can have

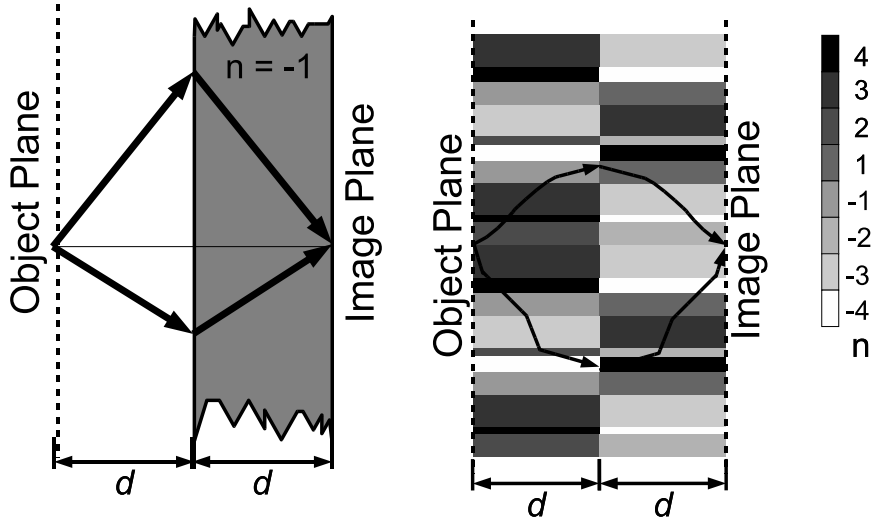

Figure 9.5 A flat slab of $n = -1$ of thickness d along with a slab of vacuum of thickness d is a special case of optical complementary media. A pair of complementary media nullifies the effects of each other for the passage of light. The gray scales for figure on the right suggests a possible scale for the refractive indices. The paths for the propagating modes in the media are not straight lines in general.

an arbitrary variation along the transverse direction, and yet we can have perfect focusing if certain conditions are satisfied.

Let us consider the region $0 < z < d$ to be filled by a medium of one kind and the region $d < z < 2d$ to be filled with a second medium. It has been shown in Pendry and Ramakrishna (2003) that the electromagnetic fields on the $z = 0$ object plane are reproduced at the image plane at $z = 2d$, if the perfect lens conditions are generalized to

$$\varepsilon_1 = +\varepsilon(x, y), \qquad \mu_1 = +\mu(x, y), \qquad \forall \quad 0 < z < d, \tag{9.11a}$$

$$\varepsilon_2 = -\varepsilon(x, y), \qquad \mu_2 = -\mu(x, y), \qquad \forall \quad d < z < 2d, \tag{9.11b}$$

where $\varepsilon(x, y)$ and $\mu(x, y)$ are some arbitrary functions of x and y and can take positive or negative values (See Fig. 9.5 [right] for a schematic picture). We term such media *Complementary Media*. The Veselago lens shown on the left is only a special case of complementary media with no transverse variation. Upon transport through a pair of complementary media of equal thickness, radiation undergoes no change in phase or amplitude. Thus, to the world on the right side of the complementary media pair, all sources on the left side of the lens just appear transposed by a distance $2d$ forward. The presence of the complementary media pair is not felt at all and corresponds to zero optical thickness. This gives an alternative and fruitful physical picture of negative

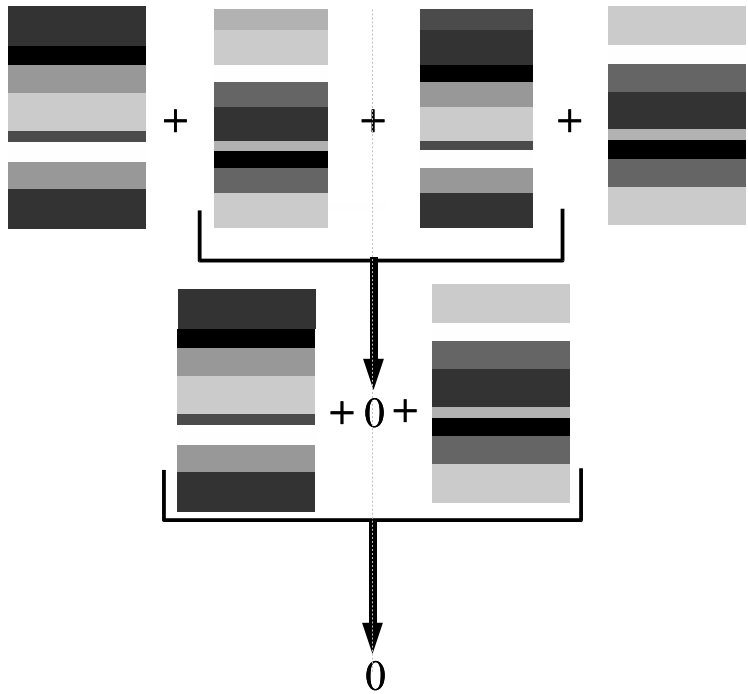

Figure 9.6 A pair of complementary media nullifies the effects of each other for the passage of light. The complementary media sum to an optical null pairwise if the system has a mirror antisymmetry about the central plane, and the entire system sums to a null. The same gray scale as in Fig. 9.5 is used to indicate the refractive indices of different regions.

refractive index media: negative refractive index media are the equivalent of "optical anti-matter" which nullify the effects of normal media on radiation. Note that we have not defined the media outside the region $0 < z < 2d$ as that is immaterial to the imaging process. Also note that the path of light in these media is not along straight lines as in homogeneous media and is schematically depicted in the figure. Effectively, this theorem states that the variation in the transverse directions is immaterial as long as the same sense of variation is present in the complementary slab.

In fact, if the media on either side of the $z = d$ plane also had material parameters that depend on z, the focusing would still be obtainable if the $z = d$ plane were a plane of anti-symmetry along the $\hat{z}$ direction. In other words, if the system is anti-symmetric about the $z = d$ plane, the complementary media can be eliminated to a null in a pairwise fashion as shown in Fig. 9.6, where the meaning of this theorem is expressed pictorially for piecewise continuous

media. In general, if

$$\varepsilon_2(x,y,2d-z) = -\varepsilon_1(x,y,z), \qquad \mu_2(x,y,2d-z) = -\mu_1(x,y,z), \quad (9.12)$$

then also the two regions behave as optically complementary and have no total effect on radiation that passes through them.

We now prove the above theorem for the general case of anisotropic dielectric and magnetic complementary media. In general, we have for the region-1,

$$\bar{\bar{\varepsilon}}_1 = \begin{pmatrix} \varepsilon_{1xx} & \varepsilon_{1xy} & \varepsilon_{1xz} \\ \varepsilon_{1yx} & \varepsilon_{1yy} & \varepsilon_{1yz} \\ \varepsilon_{1zx} & \varepsilon_{1zy} & \varepsilon_{1zz} \end{pmatrix}, \qquad \bar{\bar{\mu}}_1 = \begin{pmatrix} \mu_{1xx} & \mu_{1xy} & \mu_{1xz} \\ \mu_{1yx} & \mu_{1yy} & \mu_{1yz} \\ \mu_{1zx} & \mu_{1zy} & \mu_{1zz} \end{pmatrix}. \quad (9.13)$$

Similarly, for the region-2 ($d < z < 2d$),

$$\bar{\bar{\varepsilon}}_2 = \begin{pmatrix} \varepsilon_{2xx} & \varepsilon_{2xy} & \varepsilon_{2xz} \\ \varepsilon_{2yx} & \varepsilon_{2yy} & \varepsilon_{2yz} \\ \varepsilon_{2zx} & \varepsilon_{2zy} & \varepsilon_{2zz} \end{pmatrix}, \qquad \bar{\bar{\mu}}_2 = \begin{pmatrix} \mu_{2xx} & \mu_{2xy} & \mu_{2xz} \\ \mu_{2yx} & \mu_{2yy} & \mu_{2yz} \\ \mu_{2zx} & \mu_{2zy} & \mu_{2zz} \end{pmatrix}. \quad (9.14)$$

Note that the tensorial components are specified functions of the transverse coordinates (x, y). The electromagnetic fields have to satisfy the Maxwell equations:

$$\nabla \times \mathbf{E} = \mathrm{i}\omega\mu_0 \bar{\bar{\mu}}\, \mathbf{H}, \qquad \nabla \times \mathbf{H} = -\mathrm{i}\omega\varepsilon_0 \bar{\bar{\varepsilon}}\, \mathbf{E}. \quad (9.15)$$

Decomposing the fields into the Fourier components in the two slabs,

$$\mathbf{E}_1(x,y,z) = \exp(\mathrm{i}k_{1z}z) \sum_{k_x,k_y} \exp[\mathrm{i}(k_x x + k_y y)] \begin{pmatrix} E_{1x}(k_x,k_y) \\ E_{1y}(k_x,k_y) \\ E_{1z}(k_x,k_y) \end{pmatrix}, \quad (9.16a)$$

$$\mathbf{E}_2(x,y,z) = \exp(\mathrm{i}k_{2z}z) \sum_{k_x,k_y} \exp[\mathrm{i}(k_x x + k_y y)] \begin{pmatrix} E_{2x}(k_x,k_y) \\ E_{2y}(k_x,k_y) \\ E_{2z}(k_x,k_y) \end{pmatrix}, \quad (9.16b)$$

where the Bloch conditions can be assumed. Substituting these fields into the Maxwell equations and separating out the components, we have

$$k_y E_{1z}(k_x,k_y) - k_{1z} E_{1y}(k_x,k_y) = -\omega\mu_0 \sum_{k'_x,k'_y} [\mu_{1xx}(k_x,k_y;k'_x,k'_y) H_{1x}(k'_x,k'_y) + \mu_{1xy}(k_x,k_y;k'_x,k'_y) H_{1y}(k'_x,k'_y) + \mu_{1xz}(k_x,k_y;k'_x,k'_y) H_{1z}(k'_x,k'_y)], \quad (9.17a)$$

$$k_{1z} E_{1x}(k_x,k_y) - k_x E_{1z}(k_x,k_y) = -\omega\mu_0 \sum_{k'_x,k'_y} [\,\mu_{1yx}(k_x,k_y;k'_x,k'_y) H_{1x}(k'_x,k'_y) + \mu_{1yy}(k_x,k_y;k'_x,k'_y) H_{1y}(k'_x,k'_y) + \mu_{1yz}(k_x,k_y;k'_x,k'_y) H_{1z}(k'_x,k'_y)], \quad (9.17b)$$

$$k_x E_{1y}(k_x,k_y) - k_y E_{1x}(k_x,k_y) = -\omega\mu_0 \sum_{k'_x,k'_y} [\mu_{1zx}(k_x,k_y;k'_x,k'_y) H_{1x}(k'_x,k'_y) + \mu_{1zy}(k_x,k_y;k'_x,k'_y) H_{1y}(k'_x,k'_y) + \mu_{1zz}(k_x,k_y;k'_x,k'_y) H_{1z}(k'_x,k'_y)], \quad (9.17c)$$

and

$$k_y H_{1z}(k_x,k_y) - k_{1z} H_{1y}(k_x,k_y) = \omega\varepsilon_0 \sum_{k'_x,k'_y} [\varepsilon_{1xx}(k_x,k_y;k'_x,k'_y)E_{1x}(k'_x,k'_y) + \varepsilon_{1xy}(k_x,k_y;k'_x,k'_y)E_{1y}(k'_x,k'_y) + \varepsilon_{1xz}(k_x,k_y;k'_x,k'_y)E_{1z}(k'_x,k'_y)], \tag{9.18a}$$

$$k_{1z} H_{1x}(k_x,k_y) - k_x H_{1z}(k_x,k_y) = \omega\varepsilon_0 \sum_{k'_x,k'_y} [\varepsilon_{1yx}(k_x,k_y;k'_x,k'_y)E_{1x}(k'_x,k'_y) + \varepsilon_{1yy}(k_x,k_y;k'_x,k'_y)E_{1y}(k'_x,k'_y) + \varepsilon_{1yz}(k_x,k_y;k'_x,k'_y)E_{1z}(k'_x,k'_y)], \tag{9.18b}$$

$$k_x H_{1y}(k_x,k_y) - k_y H_{1x}(k_x,k_y) = \omega\varepsilon_0 \sum_{k'_x,k'_y} [\varepsilon_{1zx}(k_x,k_y;k'_x,k'_y)E_{1x}(k'_x,k'_y) + \varepsilon_{1zy}(k_x,k_y;k'_x,k'_y)E_{1y}(k'_x,k'_y) + \varepsilon_{1zz}(k_x,k_y;k'_x,k'_y)E_{1z}(k'_x,k'_y)]. \tag{9.18c}$$

Now consider the substitutions for the field quantities:

$$E_{2x}(k_x,k_y) = E_{1x}(k_x,k_y), \tag{9.19a}$$
$$E_{2y}(k_x,k_y) = E_{1y}(k_x,k_y), \tag{9.19b}$$
$$E_{2z}(k_x,k_y) = -E_{1z}(k_x,k_y), \tag{9.19c}$$
$$H_{2x}(k_x,k_y) = H_{1x}(k_x,k_y), \tag{9.19d}$$
$$H_{2y}(k_x,k_y) = H_{1y}(k_x,k_y), \tag{9.19e}$$
$$H_{2z}(k_x,k_y) = -H_{1z}(k_x,k_y), \tag{9.19f}$$
$$k_{2z} = -k_{1z}, \tag{9.19g}$$

and for the material parameters, the substitutions

$$\bar{\bar{\varepsilon}}_2(k_x,k_y;k'_x,k'_y) = \begin{pmatrix} -\varepsilon_{1xx}(k_x,k_y;k'_x,k'_y) & -\varepsilon_{1xy}(k_x,k_y;k'_x,k'_y) & +\varepsilon_{1xz}(k_x,k_y;k'_x,k'_y) \\ -\varepsilon_{1yx}(k_x,k_y;k'_x,k'_y) & -\varepsilon_{1yy}(k_x,k_y;k'_x,k'_y) & +\varepsilon_{1yz}(k_x,k_y;k'_x,k'_y) \\ +\varepsilon_{1zx}(k_x,k_y;k'_x,k'_y) & +\varepsilon_{1zy}(k_x,k_y;k'_x,k'_y) & -\varepsilon_{1zz}(k_x,k_y;k'_x,k'_y) \end{pmatrix}, \tag{9.20a}$$

$$\bar{\bar{\mu}}_2(k_x,k_y;k'_x,k'_y) = \begin{pmatrix} -\mu_{1xx}(k_x,k_y;k'_x,k'_y) & -\mu_{1xy}(k_x,k_y;k'_x,k'_y) & +\mu_{1xz}(k_x,k_y;k'_x,k'_y) \\ -\mu_{1yx}(k_x,k_y;k'_x,k'_y) & -\mu_{1yy}(k_x,k_y;k'_x,k'_y) & +\mu_{1yz}(k_x,k_y;k'_x,k'_y) \\ +\mu_{1zx}(k_x,k_y;k'_x,k'_y) & +\mu_{1zy}(k_x,k_y;k'_x,k'_y) & -\mu_{1zz}(k_x,k_y;k'_x,k'_y) \end{pmatrix}. \tag{9.20b}$$

These fields resolve the Maxwell equations in region-2 for the new material parameter tensors and the boundary conditions on the continuity of the electromagnetic fields across the interface of the slabs at $z = d$ are also satisfied.

Hence we have the field

$$E(x, y, z = 2d) = E(x, y, z = d) \exp(-ik_z d) = E(x, y, z = 0), \tag{9.21}$$

i.e., the fields at $z = 0$ are reproduced at $z = 2d$. The fields are exactly repeated in region-2 but in the opposite order along $\hat{z}$. For an arbitrary source in general, we have a sum over the wave-vector k_z. Since the theorem holds individually for each k_z, it also holds for the sum. This completes the proof of this theorem that generalizes the perfect lens effect to spatially varying complementary media. Thus the sufficient condition for the optical complementarity is that the material parameters for the second complementarity slab should be related to the first by

$$\bar{\bar{\varepsilon}}_2 = \begin{pmatrix} -\varepsilon_{1xx} & -\varepsilon_{1xy} & +\varepsilon_{1xz} \\ -\varepsilon_{1yx} & -\varepsilon_{1yy} & +\varepsilon_{1yz} \\ +\varepsilon_{1zx} & +\varepsilon_{1zy} & -\varepsilon_{1zz} \end{pmatrix}, \qquad \bar{\bar{\mu}}_2 = \begin{pmatrix} -\mu_{1xx} & -\mu_{1xy} & +\mu_{1xz} \\ -\mu_{1yx} & -\mu_{1yy} & +\mu_{1yz} \\ +\mu_{1zx} & +\mu_{1zy} & -\mu_{1zz} \end{pmatrix}, \tag{9.22}$$

where all the tensorial components are arbitrary well-behaved functions of the transverse coordinates. Numerical simulations have confirmed the focusing for complementary media with transverse spatial variation up to the accuracy of the calculations (Pendry and Ramakrishna 2003).

9.2.1 Proof based on the symmetries of the Maxwell equations

A simple and elegant proof for the generalized perfect lens theorem with anisotropic media can be deduced from the symmetry of the Maxwell equations. Consider the Maxwell equations

$$\nabla \times \mathbf{E} = \mathrm{i}\omega \mathbf{B}, \tag{9.23a}$$

$$\nabla \times (\mu^{-1}\mathbf{B}) = -\mathrm{i}\omega\varepsilon\mathbf{E}, \tag{9.23b}$$

where by ε and μ we imply the actual permittivity and actual magnetic permeability and not the relative ones (for use in this proof alone). Some transformations that leave these equations invariant are:

S1: $\mathbf{E} \to \mathcal{A}\mathbf{E}, \mathbf{B} \to \mathcal{A}\mathbf{B}, \mu^{-1} \to \mathcal{A}\mu^{-1}\mathcal{A}^{-1}, \varepsilon \to \mathcal{A}\varepsilon\mathcal{A}^{-1}$, where $\mathcal{A}$ is invertible and an element of $GL_3(\mathbf{R})$ (the group of 3×3 linear operators). ... *Generalized conformal invariance.*

S2: $\mathbf{E} \to -\varepsilon^{-1}\mathbf{B}, \mathbf{B} \to \mu\mathbf{E}$, or $\mathbf{E} \to \mu^{-1}\mathbf{B}, \mathbf{B} \to -\varepsilon\mathbf{E}$ (*iff* $\mu = \varepsilon$) ... *Generalized duality.*

S3: $\mu \to \alpha\mu, \varepsilon \to \varepsilon/\alpha$ where α is a non-zero scalar.

S4: $\mathbf{r} \to -\mathbf{r}$, where $\mathbf{r} = [x, y, z]$, $\mathbf{E} \to -\mathbf{E}$ ($\mathbf{B}$ is a pseudo vector) ... *Inversion.*

S5: Any additional space-time symmetries such as translational invariance etc.

The combination of any of these symmetries is again a symmetry of the system of equations. Then we can assert that *if the fields in a particular region of space can be mapped onto another region of space through the symmetry transformations S1 – S5, while preserving the respective boundary conditions, then the transformed fields solve the field equations whenever the original fields do.*

The boundary conditions here include, of course, the conditions of continuity of the tangential components of $\mathbf{E}$ and the normal component of $\mathbf{B}$ across any charge free and current free boundaries.

Let us apply these transformations to our slab in the region $-d < z < 0$ with dielectric permittivity and magnetic permeability tensors

$$\bar{\bar{\varepsilon}}_1 = \begin{pmatrix} \varepsilon_{xx} & \varepsilon_{xy} & \varepsilon_{xz} \\ \varepsilon_{yx} & \varepsilon_{yy} & \varepsilon_{yz} \\ \varepsilon_{zx} & \varepsilon_{zy} & \varepsilon_{zz} \end{pmatrix}, \qquad \bar{\bar{\mu}}_1 = \begin{pmatrix} \mu_{xx} & \mu_{xy} & \mu_{xz} \\ \mu_{yx} & \mu_{yy} & \mu_{yz} \\ \mu_{zx} & \mu_{zy} & \mu_{zz} \end{pmatrix}. \tag{9.24}$$

For propagation along the z direction and origin at the interface, let us use the symmetry operations of a reflection $S4$ ($z \to -z$) and $S3$ ($\alpha = -1$), followed by $S1$ ($\mathcal{A}$) with

$$\mathcal{A} = \begin{pmatrix} -1 & 0 & 0 \\ 0 & -1 & 0 \\ 0 & 0 & 1 \end{pmatrix}. \tag{9.25}$$

We call this sequence of operations a mirror operation. This choice of $\mathcal{A}$ preserves the continuity of $\mathbf{E}_{\|}$ and $\mathbf{B}_{\perp}$ across the $z = 0$ interface. Then the resulting complementary medium on the right for $0 < z < d$ is obtained as

$$\bar{\bar{\varepsilon}}_2 = \begin{pmatrix} -\varepsilon_{xx} & -\varepsilon_{xy} & +\varepsilon_{xz} \\ -\varepsilon_{yx} & -\varepsilon_{yy} & +\varepsilon_{yz} \\ +\varepsilon_{zx} & +\varepsilon_{zy} & -\varepsilon_{zz} \end{pmatrix}, \quad \bar{\bar{\mu}}_2 = \begin{pmatrix} -\mu_{xx} & -\mu_{xy} & +\mu_{xz} \\ -\mu_{yx} & -\mu_{yy} & +\mu_{yz} \\ +\mu_{zx} & +\mu_{zy} & -\mu_{zz} \end{pmatrix}, \tag{9.26}$$

which is the result we obtained before.

9.2.2 Contradictions between the ray picture and the full wave solutions

The generalized perfect lens theorem is a very powerful statement about the behavior of electromagnetic fields in complementary media. It is actually counter-intuitive in many ways and, interestingly, contradicts the results of a ray analysis in many cases. For example, consider the rays that are incident on a pair of slabs of complementary media shown in Fig. 9.7. The first one on the left consists of alternating rectangular regions of $n = \pm 1$. The rays can be seen to either transmit through or retro-reflect depending on the point and on the angle at which they are incident. The generalized lens theorem, however, predicts only one thing: the complementary slab pair has a transmission coefficient of unity for all plane waves regardless of their direction of incidence.

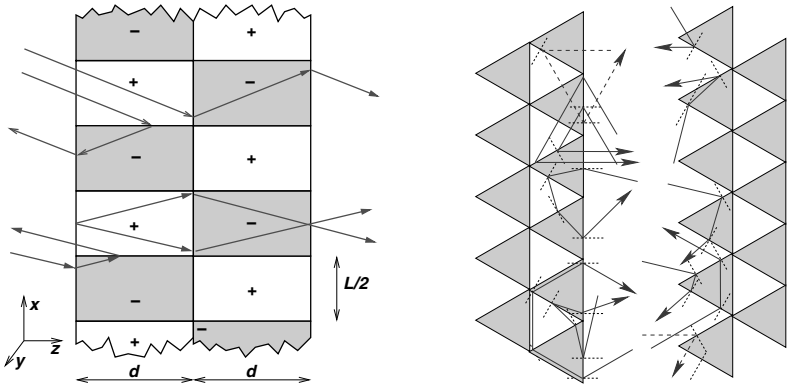

Figure 9.7 Left: Pair of complementary media slabs of thickness d each. The refractive index takes the values $n = +1$ and $n = -1$ periodically along the transverse axis (effectively part of a rectangular checkerboard) with a period of $L/2$. Rays can be seen to be either transmitted or retro-reflected. Right: Extreme example of a complementary media slab pair where each slab consists of alternating equilateral triangular regions with $n = +1$ and $n = -1$, which can be seen to reflect all rays incident upon them. Invariance along the axis normal to the plane of the figure is assumed in both cases.

The second example on the right of Fig. 9.7 shows a complementary medium slab pair composed of alternating equilateral triangular regions with $n = \pm 1$ and the invariance assumed in the direction normal to the plane is more extreme. The ray analysis reveals that every ray incident on the slab should be reflected, regardless of the direction and the point (x) on the slab at which it is incident. We do neglect here the points of singularities such as the corners for the ray analysis. The generalized lens theorem, however, predicts a perfect transmission for every wave. Thus, there is a total contradiction between the predictions of the ray picture and that of the generalized lens theorem that is based on the full solutions to the Maxwell equations. Another case consisting of a spherical cavity in an otherwise homogeneous slab of $n = \pm 1$ and its complementary slab has also been pointed out (Pendry 2004b).

The contradiction between the generalized lens theorem and the ray analyses can be worrisome at first sight. However, one has to bear in mind that the ray picture stems from a high frequency approximation of the Maxwell equations, based on the Eikonal equation (Born and Wolf 1999), while the generalized lens theorem is an exact statement. In fact, there are other instances in Optics where the ray analysis is known to fail. For example, in order to explain the case of complete reflection of light incident at an angle on a stratified medium with slowly and monotonically decreasing refractive index, one has to invoke either the total internal reflection (which involves evanescent waves for which we have no corresponding ray) or the curvature

of the wave-front associated with the wave, which again is not considered in the ray approximation.

The properties of complementary media strongly depend on the resonant surface plasmon states on the interfaces and on their interactions, whereas these localized resonances are not accounted for in the ray picture. The strange transmittive power of the piecewise continuous complementary media presented here can be traced to the propagation of surface plasmons on their interfaces and the scattering of these interface states from the corners. These are another instance of extraordinary transmission that is possible with metamaterials and which holds for all incident waves – propagating and evanescent. The mechanism of plasmonic guidance involved here via the interfaces between positive and negative index media differs substantially from the extraordinary transmission through subwavelength holes in thick metallic films that have become so popular in recent times (Ebbesen et al. 1998, Barnes et al. 2003).

Given the simplicity of the ray picture compared to full wave calculations, one is likely to be tempted to use the ray analysis as the first line of attack. In many cases the ray picture does yield some useful information about the modes of the system. However, we have seen that the ray analysis of situations involving localized resonances can lead to incorrect conclusions. Hence, any prediction based on the ray analysis in the case of complementary media has to be carefully checked by a full wave analysis.

9.3 The perfect lens in other geometries

Beyond a point, the planar geometry of the slab lens and the layered lens can be quite constraining. For example, the size of the image is bound to be the same as the object, and the system cannot focus a beam of light into a tight spot. Lenses in Optics are used for a multitude of effects and most importantly to magnify or demagnify the image of a source. In the slab lens the unit magnification comes about primarily due to the translational invariance along the transverse directions due to which the parallel wave-vector components (k_x, k_y) are conserved. That is why traditional Optical lenses have curved surfaces – the translational invariance is broken, and the distribution of parallel wave-vectors can be changed. Then the image can have a different transverse size than the source.

Obtaining super-lenses with curved surfaces is not straightforward. The performance and subwavelength image resolution of a super-lens is directly related to the near-degeneracy of the surface plasmons on the interfaces of the super-lens. In general, curved surfaces have a very different surface plasmon spectrum than the flat surfaces discussed so far. The only known exception

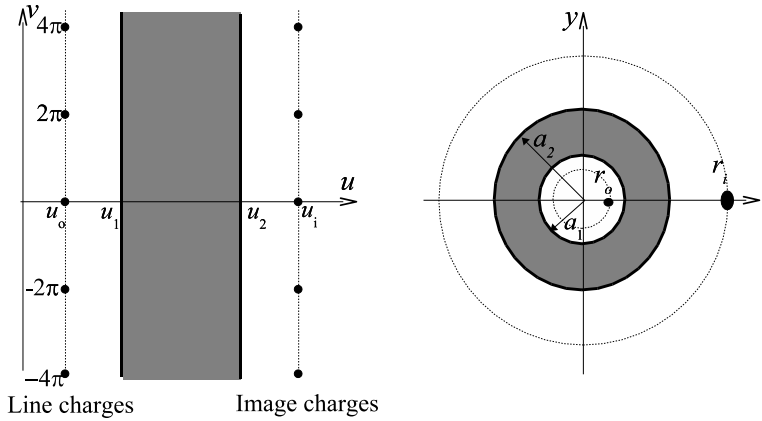

Figure 9.8 Left: Imaging by a slab lens of a set of periodically placed charges at $u = u_o$ and $v = 2m\pi$ in the z' plane. Right: Upon a conformal mapping $z' = \ln z$, the parallel lines go into concentric circles and the periodically placed charges map into one charge. The image of the charge is formed outside the cylindrical annulus of negative dielectric permittivity indicated by a gray shadow.

is approximate: a cylindrical surface with negative, homogeneous dielectric permittivity has a nearly degenerate plasmon dispersion in the quasi-static limit, i.e., when the cylinder is very thin compared to the wavelength. It has been shown (Pendry and Ramakrishna 2002) that a cylindrical shell of negative dielectric permittivity ($\varepsilon = -1$) can act as a super-lens in the quasi-static limit for TM polarization whereby it transfers inside (outside) the image of a line charge placed outside (inside) it. The proof of this is most easily given by utilizing a conformal map

$$z' = \ln z, \tag{9.27}$$

where $z = x + \mathrm{i}y$ and $z' = u + \mathrm{i}v$ for the solutions of the Laplace equation (extreme near-field limit) for the slab geometry. Here in the z'-plane, u is the optical axis of the slab lens and v is the transverse direction. The transformation maps lines parallel to the v axis into concentric circles in the z plane, hence mapping a set of periodic line charges along the line $u = u_0$ into a single charge of the same magnitude. The positions of the source, image, and the radii of the cylindrical shell are given by

$$u_o = \ln r_o, \quad u_1 = \ln a_1, \quad u_2 = \ln a_2, \quad u_i = \ln r_i, \tag{9.28}$$

as shown in Fig. 9.8. This lens can also be shown to have a spatial magnification of the near-field image by a factor of $(a_2/a_1)^2$.

While the Laplace equation is invariant under a conformal mapping and the solutions so obtained are valid in the extreme near-field approximation,

the Maxwell equations and the Helmholtz equations are notinvariant under a conformal map. However, we can utilize the known solutions in one geometry such as the slab geometry and map them to another geometry in a similar manner using a coordinate transformation. In the remainder of this chapter, we discuss the possibility of obtaining focusing with cylindrical lenses (Pendry 2003), spherical lenses (Pendry and Ramakrishna 2003, Ramakrishna and Pendry 2004), two-dimensional sharp corners (Pendry and Ramakrishna 2003), checkerboards and three-dimensional corners (Guenneau et al. 2005b).

9.3.1 A transformation technique

We should note that a geometric mapping via a coordinate transformation would distort space, inducing a change in the material tensors ε and μ in the transformed geometry.‡ Thus, the material parameters in the transformed geometry would be spatially varying (heterogeneous) and anisotropic in general.

Consider a general transformation of the coordinates from the Cartesian coordinates:

$$q_1 = q_1(x, y, z), \qquad q_2 = q_2(x, y, z), \qquad q_3 = q_3(x, y, z). \tag{9.29}$$

A cube in the new coordinate system would appear highly distorted in the Cartesian coordinate system. In the new coordinate system, Maxwell equations have been shown to take the form (Ward and Pendry 1996)

$$\nabla_{\mathbf{q}} \times \tilde{\mathbf{E}} = \mathrm{i}\omega\mu_0\tilde{\mu}\tilde{\mathbf{H}}, \tag{9.30a}$$

$$\nabla_{\mathbf{q}} \times \tilde{\mathbf{H}} = -\mathrm{i}\omega\varepsilon_0\tilde{\varepsilon}\tilde{\mathbf{E}}, \tag{9.30b}$$

where $\tilde{\varepsilon}$ and $\tilde{\mu}$ are, in general, some (frequency-dependent) tensors, and $\tilde{\mathbf{E}}$ and $\tilde{\mathbf{H}}$ are renormalized fields. The Maxwell equations hence preserve their form in terms of these new renormalized quantities. If (q_1, q_2, q_3) are assumed to be orthogonal, then the renormalized $\tilde{\varepsilon}$ and $\tilde{\mu}$, and fields in the new coordinate system are related to the actual material parameters and fields by

$$\tilde{\varepsilon}_i = \varepsilon_i \frac{Q_1 Q_2 Q_3}{Q_i^2}, \qquad \tilde{\mu}_i = \mu_i \frac{Q_1 Q_2 Q_3}{Q_i^2}, \tag{9.31a}$$

$$\tilde{E}_i = Q_i E_i, \qquad \tilde{H}_i = Q_i H_i, \tag{9.31b}$$

where

$$Q_i^2 = \left(\frac{\partial x}{\partial q_i}\right)^2 + \left(\frac{\partial y}{\partial q_i}\right)^2 + \left(\frac{\partial z}{\partial q_i}\right)^2. \tag{9.32}$$

‡The same principle can be used to cloak regions of spaces from external electromagnetic radiation and achieve electromagnetic invisibility, as discussed in Chapter 10.

The essential idea is to map new geometries into geometries where we know the solutions, for example, the Veselago slab lens. We can then use the known solutions of the fields to recover the fields in the new geometries as well as to define the actual inhomogeneous and anisotropic material parameter tensors in the new geometries. The essential condition for this procedure to work is, of course, that the transformation should be invertible. Since we have already assumed that we only transform to orthogonal coordinate systems, the boundary conditions on the fields are satisfied in both geometries.

In the remainder of this section, we use this coordinate transformation technique to generate super-lenses in new geometrical configurations.

9.3.2 Perfect lenses in curved geometries: cylindrical and spherical lenses

Cylindrical lenses:

To generate cylindrical lenses, let us make a transformation from the Cartesian to cylindrical coordinates:

$$x = r_0 e^{\ell/\ell_0} \cos\phi, \qquad y = r_0 e^{\ell/\ell_0} \sin\phi, \qquad z = Z, \tag{9.33}$$

where $r = r_0 e^{\ell/\ell_0}$ and $r_0,\ \ell_0$ are some scaling parameters. We obtain

$$Q_\ell = \frac{r_0}{\ell_0} e^{\ell/\ell_0}, \tag{9.34a}$$

$$Q_\phi = r_0 e^{\ell/\ell_0}, \tag{9.34b}$$

$$Q_Z = 1 \tag{9.34c}$$

for the transformation. Hence the renormalized material parameters come out to be

$$\tilde{\varepsilon}_\ell = \ell_0 \varepsilon_\ell, \qquad \tilde{\varepsilon}_\phi = \ell_0^{-1} \varepsilon_\phi, \qquad \tilde{\varepsilon}_Z = \frac{r_0^2}{\ell_0^2} \exp\left(\frac{2\ell}{\ell_0}\right) \varepsilon_z, \tag{9.35a}$$

$$\tilde{\mu}_\ell = \ell_0 \mu_\ell, \qquad \tilde{\mu}_\phi = \ell_0^{-1} \mu_\phi, \qquad \tilde{\mu}_Z = \frac{r_0^2}{\ell_0^2} \exp\left(\frac{2\ell}{\ell_0}\right) \mu_z. \tag{9.35b}$$

Choosing the scale factor $\ell_0 = 1$ and explicitly defining the material parameters in the cylindrical geometry as

$$\left.\begin{aligned} \varepsilon_r &= \mu_r = +1, \\ \varepsilon_\phi &= \mu_\phi = +1, \\ \varepsilon_z &= \mu_z = +1/r^2, \end{aligned}\right\} \qquad \forall \ \ r < a_1, \tag{9.36a}$$

$$\left.\begin{aligned} \varepsilon_r &= \mu_r = -1, \\ \varepsilon_\phi &= \mu_\phi = -1, \\ \varepsilon_z &= \mu_z = -1/r^2, \end{aligned}\right\} \qquad \forall \ \ a_1 < r < a_2, \tag{9.36b}$$

$$\left.\begin{array}{l}\varepsilon_r = \mu_r = +1,\\ \varepsilon_\phi = \mu_\phi = +1,\\ \varepsilon_z = \mu_z = +1/r^2,\end{array}\right\} \qquad \forall \;\; a_2 < r, \tag{9.36c}$$

we obtain that

$$\left.\begin{array}{l}\tilde{\varepsilon}_\ell = \tilde{\mu}_\ell = +1,\\ \tilde{\varepsilon}_\phi = \tilde{\mu}_\phi = +1,\\ \tilde{\varepsilon}_z = \tilde{\mu}_z = +1,\end{array}\right\} \quad \forall \;\; \ell < \ell_0 \ln(a_1/r_0), \tag{9.37a}$$

$$\left.\begin{array}{l}\tilde{\varepsilon}_\ell = \tilde{\mu}_\ell = -1,\\ \tilde{\varepsilon}_\phi = \tilde{\mu}_\phi = -1,\\ \tilde{\varepsilon}_z = \tilde{\mu}_Z = -1,\end{array}\right\} \quad \forall \;\; \ell_0 \ln(a_1/r_0) < \ell < \ell_0 \ln(a_2/r_0), \tag{9.37b}$$

$$\left.\begin{array}{l}\tilde{\varepsilon}_\ell = \tilde{\mu}_\ell = +1,\\ \tilde{\varepsilon}_\phi = \tilde{\mu}_\phi = +1,\\ \tilde{\varepsilon}_z = \tilde{\mu}_Z = +1,\end{array}\right\} \quad \forall \;\; \ell_0 \ln(a_2/r_0) < \ell \tag{9.37c}$$

in the ℓ, ϕ, Z coordinates. The renormalized material parameters satisfy the same conditions as the slab perfect lens in Cartesian coordinates. Hence we have actually specified a perfect lens in the cylindrical geometry through our choice of the material parameters. Note that our choice of the spatial dependence of the material parameters was done so as to obtain homogeneous renormalized $\tilde{\varepsilon}$ and $\tilde{\mu}$. Note that the z-components of the material parameter tensors are inhomogeneous and have $1/r^2$ dependence.

The new system with the specified parameters must accordingly act as a cylindrical super-lens, and transfer images in and out of the cylindrical annulus. Let us suppose that the line source is located at (r_o, ϕ_o) inside the cylindrical annulus (see Fig. 9.8). The location of the image can be obtained from the condition

$$(\ell_1 - \ell_o) - (\ell_i - \ell_2) = (\ell_2 - \ell_1) \quad \Rightarrow \quad r_i = r_o(a_2/a_1)^2, \phi_i = \phi_o. \tag{9.38}$$

All lengthscales on the image are magnified (angular magnification $\Delta\phi$) by a factor of

$$\mathcal{M} = \left(\frac{a_2}{a_1}\right)^2, \tag{9.39}$$

which is the magnification of this system. Note that the magnification or demagnification of the image holds for the near-field image as well. For example, if the fast-varying features are not amenable to interrogation by a scanning near-field microscope due to resolution limitations, one could instead try to image these fast-varying features in the magnified image. Another possibility is if $r_i = a_1$ and $r_o = a_2$, then the magnification of the image could allow coupling to the propagating modes in the region $r > a_2$ and hence allow us to project out the near-field. Another important point is that the demagnified images inside the cylindrical annulus would be more intense: this has potential consequences when we want to concentrate weak incident fields. Note that these cylindrical lens are also short-sighted in the same manner as the

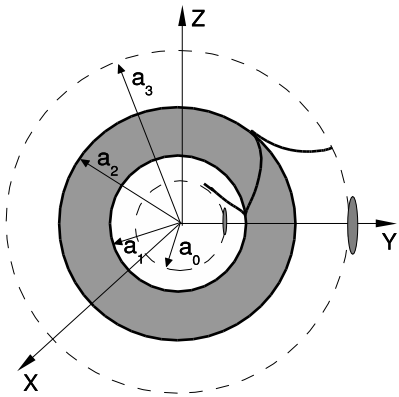

Figure 9.9 A spherical shell with negative $\varepsilon_-(r) \sim -1/r$ and $\mu_-(r) \sim -1/r$ images a source located inside the shell into the external region. The media outside have positive refractive index, but $\varepsilon_+(r) \sim 1/r$ and $\mu_+(r) \sim 1/r$. The amplification inside the spherical shell of the otherwise decaying field is schematically shown. (Reproduced with permission from Ramakrishna (2005). © 2005, Institute of Physics Publishing, U.K.)

slab lens is: they can only focus sources from inside to the outside only when $a_1^2/a_2 < r < a_1$, and the other way around from outside to the inner world when the source is located in $a_2 < r < a_2^2/a_1$. Furthermore, note that for the optical axis along the ℓ direction, the generalized lens theorem predicts that the variations in the transverse ϕ, Z directions are irrelevant. Hence the medium parameters, in general, could also be arbitrary functions of ϕ and Z.

Spherical lenses:

In an analogous manner to the cylindrical lens, we can show that a spherical shell of negative index media can also act as a super-lens. Consider a shell of negative refractive index material embedded in a positive index medium as shown in Fig. 9.9. Transforming to the spherical geometry from the Cartesian geometry:

$$x = r_0 e^{\ell/\ell_0} \sin\theta \cos\phi, \qquad y = r_0 e^{\ell/\ell_0} \sin\theta \sin\phi, \qquad z = r_0 e^{\ell/\ell_0} \cos\theta, \tag{9.40}$$

where ℓ is oriented along the radial direction, $r = r_0 e^{\ell/\ell_0}$, and $r_0,\ \ell_0$ are some

scaling parameters as before. We obtain

$$Q_\ell = \frac{r_0}{\ell_0} e^{\ell/\ell_0}, \tag{9.41a}$$

$$Q_\theta = r_0 e^{\ell/\ell_0}, \tag{9.41b}$$

$$Q_\phi = r_0 e^{\ell/\ell_0} \sin\theta \tag{9.41c}$$

for the transformation. Hence the renormalized material parameters are

$$\tilde{\varepsilon}_\ell = r_0 \ell_0 e^{\ell/\ell_0} \sin\theta \; \varepsilon_\ell, \qquad \tilde{\varepsilon}_\theta = \frac{r_0}{\ell_0} e^{\ell/\ell_0} \sin\theta \; \varepsilon_\theta, \qquad \tilde{\varepsilon}_\phi = \frac{r_0 e^{\ell/\ell_0}}{\ell_0 \sin\theta} \; \varepsilon_\phi, \tag{9.42a}$$

$$\tilde{\mu}_\ell = r_0 \ell_0 e^{\ell/\ell_0} \sin\theta \; \mu_\ell, \qquad \tilde{\mu}_\theta = \frac{r_0}{\ell_0} e^{\ell/\ell_0} \sin\theta \; \mu_\theta, \qquad \tilde{\mu}_\phi = \frac{r_0 e^{\ell/\ell_0}}{\ell_0 \sin\theta} \; \mu_\phi. \tag{9.42b}$$

Note that the imaging direction that we seek is along the radial (ℓ) direction. Choosing the scale factor $\ell_0 = 1$, we explicitly define the material parameters in the spherical geometry as

$$\varepsilon_\ell = \varepsilon_\theta = \varepsilon_\phi = \varepsilon e^{-\ell/\ell_0} = \varepsilon \frac{r_0}{r} \tag{9.43a}$$

$$\mu_\ell = \mu_\theta = \mu_\phi = \mu e^{-\ell/\ell_0} = \mu \frac{r_0}{r}. \tag{9.43b}$$

Then we obtain renormalized material parameters that have no ℓ dependence:

$$\tilde{\varepsilon}_\ell = +\varepsilon r_0 \sin\theta, \qquad \tilde{\varepsilon}_\theta = +\varepsilon r_0 \sin\theta, \qquad \tilde{\varepsilon}_\phi = \frac{+\varepsilon r_0}{\sin\theta}, \tag{9.44a}$$

$$\tilde{\mu}_\ell = +\mu r_0 \sin\theta, \qquad \tilde{\mu}_\theta = +\mu r_0 \sin\theta, \qquad \tilde{\mu}_\phi = \frac{+\mu r_0}{\sin\theta}. \tag{9.44b}$$

If the quantities ε and μ take the values $+1$ in the the regions $\ell < \ell_0 \ln(a_1/r_0)$ and $\ell_0 \ln(a_2/r_0) < \ell$, and the value -1 for $\ell_0 \ln(a_1/r_0) < \ell < \ell_0 \ln(a_2/r_0)$, then the renormalized material parameters have the required complementary behavior with no variation along the radial (imaging) direction and only a variation along the transverse (θ) direction. Hence we conclude that this system, which has isotropic but inhomogeneous ($\sim 1/r$) material parameters, acts as a spherical super-lens. Note here that it is the generalized lens theorem for complementary media with transverse variation that allows us to make this conclusion. Once again it is straightforward to show that the image of a source located at (r_o, θ_o, ϕ_o) appears at (r_i, θ_i, ϕ_i) where

$$r_i = r_o (a_2/a_1)^2, \qquad \theta_i = \theta_o, \qquad \phi_i = \phi_o, \tag{9.45}$$

and that the system has a magnification given by $\mathcal{M} = \left(\frac{a_2}{a_1}\right)^2$.

Actually this result can also be obtained by a more conventional but tedious calculation. In order to convince the reader of the considerable simplicity and

power of the transformation technique, we present this more conventional calculation (Ramakrishna and Pendry 2004) here which confirms our earlier result for the spherical shell. We consider a spherical system whose ε and μ have a variation of $1/r$ along the radial direction. Under the circumstances of spherical symmetry, it is sufficient to specify the quantities $(\mathbf{r}\cdot\mathbf{E})$ and $(\mathbf{r}\cdot\mathbf{H})$, which constitutes a full solution to the problem.

Consider the TM polarized modes $\mathbf{r}\cdot\mathbf{H}=0$, in which case only the electric fields have a radial component E_r. Operating on the Maxwell equation by ∇,

$$\begin{aligned}\nabla\times\nabla\times\mathbf{E} &= \mathrm{i}\omega\mu_0\nabla\times[\mu(\mathbf{r})\mathbf{H}]\,,\\ &= \frac{\omega^2}{c^2}\mu(\mathbf{r})\varepsilon(\mathbf{r})\mathbf{E}+\mathrm{i}\omega\frac{\nabla\mu(\mathbf{r})}{\mu(\mathbf{r})}\times\nabla\times\mathbf{E},\end{aligned}\tag{9.46}$$

and we have

$$\nabla\cdot\mathbf{D}=\nabla\cdot[\varepsilon(\mathbf{r})\mathbf{E}]=\nabla\varepsilon(\mathbf{r})\cdot\mathbf{E}+\varepsilon(\mathbf{r})\nabla\cdot\mathbf{E}=0.\tag{9.47}$$

If we assume $\varepsilon(\mathbf{r})=\varepsilon(r)$ and $\mu(\mathbf{r})=\mu(r)$, we have

$$\nabla\cdot\mathbf{E}=-\frac{\varepsilon'(r)}{r\varepsilon(r)}\mathbf{r}\cdot\mathbf{E}=-\frac{\varepsilon'(r)}{r\varepsilon(r)}(rE_r),\tag{9.48}$$

where the prime indicates the derivative with respect to the argument shown in the parenthesis. We note the following two useful identities for subsequent use:

$$\nabla\times\nabla\times\mathbf{E}=\nabla(\nabla\cdot\mathbf{E})-\nabla^2\mathbf{E},\tag{9.49}$$

and

$$\nabla^2(\mathbf{r}\cdot\mathbf{E})=\mathbf{r}\cdot\nabla^2\mathbf{E}+2\nabla\cdot\mathbf{E}.\tag{9.50}$$

Noting that ε only depends on r, we obtain that

$$\mathbf{r}\cdot\nabla(\nabla\cdot\mathbf{E})=-\frac{\partial}{\partial r}\left(\frac{\varepsilon'(r)}{\varepsilon(r)}(rE_r)\right)+\left(\frac{\varepsilon'(r)}{\varepsilon(r)}E_r\right).\tag{9.51}$$

Using the above four equations, we can obtain an equation for the electric field as

$$\nabla^2(rE_r)+\frac{\partial}{\partial r}\left[\frac{\varepsilon'(r)}{\varepsilon(r)}(rE_r)\right]+\frac{\varepsilon'(r)}{r\varepsilon(r)}(rE_r)+\varepsilon(r)\mu(r)\frac{\omega^2}{c^2}(rE_r)=0.\tag{9.52}$$

This equation is separable in (r,θ,ϕ) and the Spherical Harmonic functions are a solution to the angular part. Hence, the solution is $(rE_r)=U(r)Y_{lm}(\theta,\phi)$ where the radial part $U(r)$ satisfies

$$\frac{1}{r^2}\frac{\partial}{\partial r}\left(r^2\frac{\partial U}{\partial r}\right)-\frac{l(l+1)}{r^2}U+\frac{\partial}{\partial r}\left[\frac{\varepsilon'(r)}{\varepsilon(r)}U\right]+\frac{\varepsilon'(r)}{r\varepsilon(r)}U+\varepsilon(r)\mu(r)\frac{\omega^2}{c^2}U=0.\tag{9.53}$$

If we choose $\varepsilon(r) = \alpha r^p$ and $\mu(r) = \beta r^q$, we can use a trial solution $U(r) \sim r^n$ and obtain

$$[n(n+1) - l(l+1) + p(n-1) + p]r^{n-2} + \alpha\beta\omega^2/c^2 r^{p+q+n} = 0, \tag{9.54}$$

implying $p + q = -2$ and

$$n_\pm = 1/2\left[-(p+1) \pm \sqrt{(p+1)^2 + 4l(l+1) - 4\alpha\beta\omega^2/c^2}\right]. \tag{9.55}$$

Hence the general solution can be written as

$$E_r(\mathbf{r}) = \sum_{l,m}\left[n_+ A_{lm} r^{n_+ - 1} + n_- B_{lm} r^{n_- - 1}\right] Y_{lm}(\theta, \phi), \tag{9.56}$$

and a similar solution can be obtained for the TE modes with $\mathbf{r} \cdot \mathbf{E} = 0$.

Assuming an arbitrary source at $r = a_0$, we can now write the electric fields of the TM modes in the different regions for the negative spherical shell of Fig. 2 as

$$\mathbf{E}^{(1)}(\mathbf{r}) = \sum_{l,m}\left[n_+ A^{(1)}_{lm} r^{n_+ - 1} + n_- B^{(1)}_{lm} r^{n_- - 1}\right] Y_{lm}(\theta, \phi), \qquad a_0 < r < a_1, \tag{9.57a}$$

$$\mathbf{E}^{(2)}(\mathbf{r}) = \sum_{l,m}\left[n_+ A^{(2)}_{lm} r^{n_+ - 1} + n_- B^{(2)}_{lm} r^{n_- - 1}\right] Y_{lm}(\theta, \phi), \qquad a_1 < r < a_2, \tag{9.57b}$$

$$\mathbf{E}^{(3)}(\mathbf{r}) = \sum_{l,m}\left[n_+ A^{(3)}_{lm} r^{n_+ - 1} + n_- B^{(3)}_{lm} r^{n_- - 1}\right] Y_{lm}(\theta, \phi), \qquad a_2 < r < \infty, \tag{9.57c}$$

and similarly for the magnetic fields. Note that the $B^{(1)}_{lm}$ correspond to the field components of the source located at $r = a_0$. For causal solutions, $A^{(3)}_{lm} = 0$. Satisfying the boundary conditions for the fields, and under the conditions $p = -1$, $q = -1$, $\varepsilon_+(a_1) = -\varepsilon_-(a_1)$, and $\varepsilon_+(a_2) = -\varepsilon_-(a_2)$, we have

$$A^{(1)}_{lm} = 0, \tag{9.58a}$$

$$A^{(2)}_{lm} = \left(\frac{1}{a_1^2}\right)^{\sqrt{l(l+1) - \alpha\beta\omega^2/c^2}} B^{(1)}_{lm}, \qquad B^{(2)}_{lm} = 0, \tag{9.58b}$$

$$B^{(3)}_{lm} = \left(\frac{a_2^2}{a_1^2}\right)^{\sqrt{l(l+1) - \alpha\beta\omega^2/c^2}} B^{(1)}_{lm}. \tag{9.58c}$$

The lens-like property of the system becomes clear by writing the field outside the spherical shell as

$$E^{(3)}_r = \frac{1}{r}\left[\frac{a_2^2}{a_1^2} r\right]^{\sqrt{l(l+1) - \alpha\beta\omega^2/c^2}} B^{(1)}_{lm} Y_{lm}(\theta, \phi). \tag{9.59}$$

Hence apart from a scaling factor of $1/r$, the fields on the sphere $r = a_3 = (a_2^2/a_1^2)a_0$ are identical to the fields on the sphere $r = a_0$. We also have a spatial magnification in the image by a factor of a_2^2/a_1^2. Similar to the cylindrical lens, this spherical lens is able to image sources that are also located only within a finite distance of the negative spherical shell. Note that the positive medium outside the shell is also required to have spatially varying material parameters that vary as $1/r$. In the presence of finite dissipation, using the ideas of the asymmetric lens (Ramakrishna et al. 2002), we can terminate the spatially varying media at some finite but large distance away from the spherical shell.

Let us note a couple of points about the above perfect lens solutions in the spherical geometry. First, for $r > a_3$, i.e., points outside the image surface, the fields appear as if the source were located on the spherical image surface ($r = a_3$). However, this is not true for points $a_2 < r < a_3$ within the image surface. Second, note that our imaging direction is along r and ε and μ can be an arbitrary function of θ and ϕ with the only condition of complementarity between the negative and positive regions. We can, however, reach this conclusion only by recourse to the generalized lens theorem and it cannot be straightforwardly obtained from the conventional calculation. Third, given that $\varepsilon_-(a_2) = -\varepsilon_+(a_2)$, we have the perfect lens solutions if and only if $n_+ = -n_-$, which implies that $p = -1$ in Eq. (9.55). Although the solutions given by Eq. (9.56) occur in any medium with $\varepsilon\mu \sim 1/r^2$, the perfect lens solutions work for both polarizations only if $\varepsilon \sim \mu \sim 1/r$. Here we have written down the solutions for the TM modes. The solutions for the TE modes can be similarly obtained. A choice of $\varepsilon \sim 1/r^2$ enables focusing for only the TM modes, and $\mu \sim 1/r^2$ enables focusing of only the TE modes.

Again there is a considerable simplification that is possible in the extreme near-field limit (Ramakrishna and Pendry 2004) in which case the imaging for the TM modes becomes independent of the magnetic permeability and only requires $\varepsilon_- \sim -1/r^2$. Similarly, the TE modes become independent of the ε and the only condition is that $\mu_- \sim -1/r^2$. Further, the constraint that the positive media outside also be spatially varying can be dropped. In this limit it can be shown that the largest multipole that can be resolved is again limited by dissipation in the NRM and is approximately (Ramakrishna and Pendry 2004)

$$l_{\max} \simeq \frac{\ln\{3\varepsilon_1\varepsilon_3/[\varepsilon_i(a_1)\varepsilon_i(a_2)]\}}{2\ln(a_2/a_1)}, \tag{9.60}$$

where $\varepsilon_1 = -\mathrm{Re}(\varepsilon_-(a_1))$ and $\varepsilon_3 = -\mathrm{Re}(\varepsilon_-(a_2))$ for the perfect lens conditions and $\varepsilon_i(r) \sim 1/r^2$ is the imaginary part of the permittivity for the negative medium shell.

A fundamental issue that comes up for the spherical or cylindrical lenses is: what do we mean by complementarity and equal thickness? For example, how would the medium within the complementary layers appear to an observer external to the complementary spherical regions? Consider the two

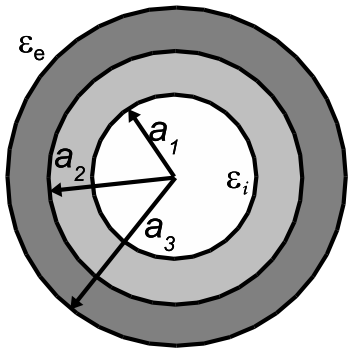

Figure 9.10 A pair of spherical complementary shells cancel each other. The two complementary shells are shown by different shades of gray.

complementary spherical regions shown in Fig. 9.10 by different shades of gray. Let (ε_e, μ_e) and (ε_i, μ_i) be the material parameters in the regions external and internal to the complementary layers, respectively. We first note that the condition of complementarity in the (ℓ, θ, ϕ) space would just imply that $\ell_3 - \ell_2 = \ell_2 - \ell_1$, which simply translates to $a_3 = a_2^2/a_1$. In the context of the generalized lens theorem in the Cartesian geometry, for an observer to the right of the layers, we could just cut out the complementary layers of equal thicknesses and move the media and the sources on the left of the layers by a distance $2d$ toward the right. In the context of the spherical lens, we could carry the operation out for the equivalent slab pair in the Cartesian geometry and then transform back into the spherical geometry. For the region beyond the complementary layers, i.e., $r > a_2$, this only amounts to undoing the original transformation and we obtain

$$\left.\begin{array}{l} \varepsilon_e^{\rm eq} = \varepsilon_e(r), \\ \mu_e^{\rm eq} = \mu_e(r), \end{array}\right\} \quad \forall \quad r > a_3. \tag{9.61}$$

However for the points $r < a_3$, the material that was originally inside the inner sphere $r < a_1$ has to now shift into the region $r < a_3$. Hence the new equivalent parameters for this region $r < a_3$ would be

$$\left.\begin{array}{l} \varepsilon_i^{\rm eq} = \frac{a_1}{a_3}\varepsilon_i(\frac{a_1}{a_3}r), \\ \mu_i^{\rm eq} = \frac{a_1}{a_3}\mu_i(\frac{a_1}{a_3}r), \end{array}\right\} \quad \forall \quad r < a_3. \tag{9.62}$$

We see that not only does the spatial dependence need to be rescaled but also the magnitudes of ε_i and μ_i need to be adjusted to account for this transformation.

9.3.3 Hyperlens: a layered curved lens

We have seen that super-lenses that utilize the excitation of the surface plasmons have a limitation in that the image resolution is deteriorated by the presence of dissipation. One way to overcome this limitation is to simply use the idea of the layered lens in curved geometries. Even if we have resonances, dissipation does not affect the obtainable resolution significantly because the amplitudes of the modes are kept small. Another possibility is to use the indefinite anisotropy of the layered system as was explained in Section 9.1.2. A lens whose function crucially stems from this anisotropy and depends on the hyperbolic nature of the dispersion has been termed a hyperlens (Jacob et al. 2006).

Similar to the expansion in plane waves $\exp(ik_x x)$ in Cartesian coordinates, the fields on a cylindrical surface $r = r_o$ can be expanded in the periodic functions $\exp(\pm im\phi)$ where m is a positive integer. In an isotropic dielectric medium, one can write for the dispersion in terms of the radial and azimuthal components of the wave vectors:

$$k_r^2 + k_\phi^2 = \varepsilon\omega^2/c^2. \tag{9.63}$$

The azimuthal wave-vector $k_\phi = m/r$ and decays in magnitude at large r. For any given m, there is a radius below which the k_r becomes imaginary and the amplitude of the mode is exponentially small for points within this radial distance. Hence if a small scattering object (with fine variation along ϕ) is placed at a small radial distance, the coupling to the large m modes that accurately describes the fast variation with ϕ becomes small and the near-field information does not propagate away. However, this would be different if one had a hyperbolic dispersion in the medium.

Consider a concentrically stratified medium made of alternative layers of silver (a negative dielectric medium) and a positive index medium as shown in Fig. 9.11. The layering creates an anisotropy for both field components, normal and parallel to the interfaces. The medium can be considered to be anisotropic with different ε_r and ε_ϕ in the effective medium limit of small layer thickness. It has been shown before that these two components can have opposite signs. We have seen in Section 2.5 that at low frequencies, $\varepsilon_\phi < 0$ and $\varepsilon_r > 0$, while at high frequencies the converse is true. In either case, the dispersion equation becomes hyperbolic, but has a low wave-vector cutoff in the first low frequency case, while there is no cutoff in the second high frequency case. In the second case, the dispersion equation is

$$\frac{k_r^2}{\varepsilon_\phi} - \frac{m^2}{r^2|\varepsilon_r|} = \mu_z \frac{\omega^2}{c^2}. \tag{9.64}$$

Thus, the large m modes do not become evanescent here for any value of m (this would be valid as far as the effective medium picture works). Hence the higher order m modes of the scattering object can couple to propagating modes in the cylinder and can propagate radially away, thus transferring

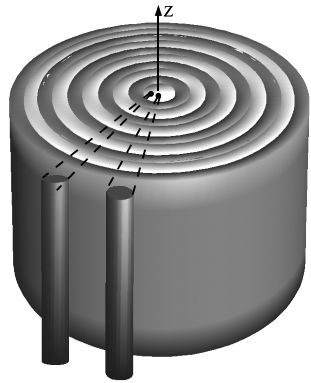

Figure 9.11 A cylindrically layered medium with alternate cylindrical layers of a negative dielectric medium (gray) and a positive medium (white) acts as an indefinite effective medium. This can be utilized to project out the near-field information of two small sources embedded within the innermost layer to the space outside the layered cylindrical system. The image so produced has a magnification and may be outcoupled to the far-field propagating modes easily.

the near-field information to much larger radial points. There would be a magnification in the image formed at larger radial distances by the ratio of the tangential wave-vectors at the source and image points, which translates to the number $\mathcal{M} = r_i/r_o$. At much larger radial points, since k_ϕ is now a small quantity, one can actually outcouple these modes to propagating modes and image them using conventional optics. The hyperlens is limited again only by the levels of dissipation in the silver, which damps out the waves as they propagate radially outward. Another critical issue is the quality and the surface roughness of the silver layers, which need to be exceptionally good for implementing the hyperlens. The hyperlens that combines the properties of the layered effective medium and the cylindrical (and in principle, spherical) lens represents an exciting implementation that utilizes the hyperbolic nature of dispersion in indefinite media to full advantage and allows for the far-field imaging of highly subwavelength sized sources.

The idea of the hyperlens has been demonstrated experimentally (Liu et al. 2007) with 16 alternating layers of silver and alumina (35 nm thickness each) deposited on the inside of a semi-cylindrical cavity on a quartz substrate. The system with radiation of about 364 nm wavelength could produce a magnified image outside the layered cylinder of two 35-nm-thick lines placed 150 nm apart inside the cylindrical layers. The spacing between the lines in the magnified image was 350 nm, which is resolvable by conventional optical microscopes. Thus, subwavelength information of $\lambda/2.5$ was propagated out by a distance of more than 3λ, which is a very significantly large distance.

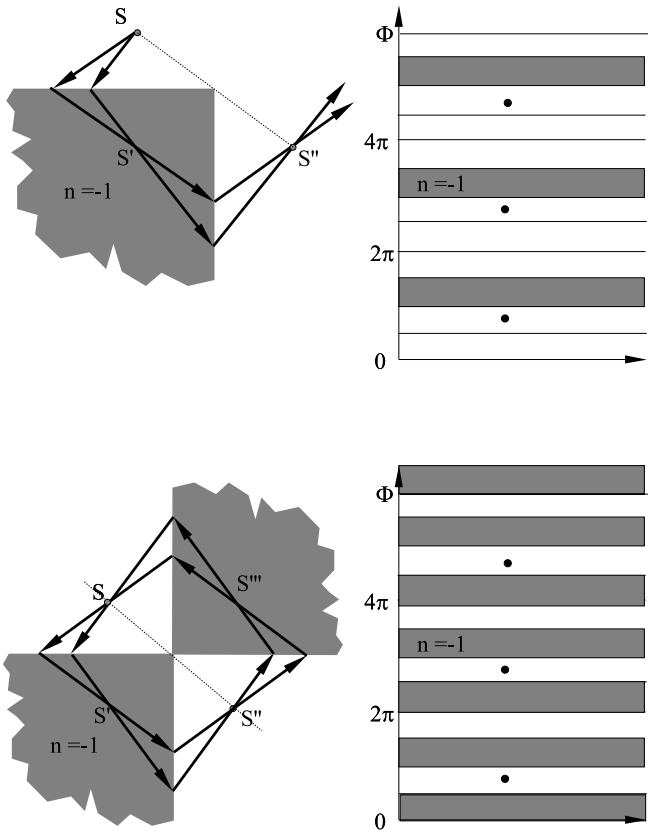

Figure 9.12 Top: (Left) A 90° wedge (corner) of negative refractive index acts as a lens with an image forming at a point in free space across the corner and inside the negative index wedge. This can be mapped into the periodic layered system with periodically placed sources shown on the right. Bottom: (Left) Two 90° wedges of negative refractive index ($n = -1$) with the corners touching can act as an open resonator. Images form in each quadrant of space and the fourth image gets focused back onto the source. This system can also be mapped into a periodic layered system of negative index slabs with periodically placed sources shown on the right.

9.3.4 Perfect two-dimensional corner lens

In the case of the cylindrical and the spherical lens we chose the radial direction as the imaging direction. An interesting variation can be obtained if one chooses instead the azimuthal ϕ direction for imaging. Sharp corners have very interesting electromagnetic properties. Even the electrostatic properties are rich, with the electrostatic fields showing a divergence in as one

approaches the singular point (Jackson 1999). Consider a wedge-shaped piece of a semi-infinite negative refractive index material with $n = -1$ shown in Fig. 9.12 with invariance along the axis normal to the plane of the figure. A ray diagram shows that the properties of negative index wedges are interesting and reveals the possibility of imaging a source across the 90^o corner as shown in Fig. 9.12. Negative refraction reverses the direction of the rays and causes a real image to form on the other side of the corner. Compare the similarities of this system to a corner reflector where a source placed inside the corner would generate an apparent image across the corner.

In fact combining two such wedges of negative refractive index medium that just touch at the corners as shown in Fig. 9.12 (bottom panel) makes it even more interesting: classical rays emanating from a source placed in any one of the quadrants are returned back to the source point (Notomi 2002). Thus, the ray picture suggests that the double corner can act as an open resonator. However, we have seen that the ray picture cannot be completely relied upon with complementary media. Hence it is desirable to have a full wave calculation to confirm the imaging properties of such a system.

Using the transformation technique and the generalized lens theorem for complementary media, it has been demonstrated (Pendry and Ramakrishna 2003) that the images formed in the above two cases are perfect in the sense that they involve both the propagating and the near-field modes of the source. Consider the periodic arrangements of slabs shown beside the corners with material parameters:

$$\varepsilon(\phi) = \mu(\phi) = \begin{cases} +1 & \forall \quad -\pi/2 < \phi < \pi, \\ -1 & \forall \quad -\pi < \phi < -\pi/2 \end{cases} \tag{9.65}$$

in the first case (a) of a single corner, and

$$\varepsilon(\phi) = \mu(\phi) = \begin{cases} +1 & \forall \quad -\pi/2 < \phi < 0 \ \text{ and } \ \pi/2 < \phi < \pi, \\ -1 & \forall \quad -\pi < \phi < -\pi/2 \ \text{ and } \ 0 < \phi < \pi/2, \end{cases} \tag{9.66}$$

in the second case (b) of the double corner lens. We assume invariance in the direction normal to the plane. Note that a source is placed in the second quadrant. It is easily seen that the layered medium periodic stack of negative refractive index can be mapped onto the corners of negative index using the transformation to cylindrical coordinates:

$$x = r_0 e^{\ell/\ell_0} \cos\phi, \qquad y = r_0 e^{\ell/\ell_0} \sin\phi, \qquad z = Z. \tag{9.67}$$

Using the transformation properties, we have

$$\tilde{\varepsilon}_\ell = \tilde{\mu}_\ell = \tilde{\varepsilon}_\phi = \tilde{\mu}_\phi = \begin{cases} +1, & \tilde{\varepsilon}_Z = \tilde{\mu}_Z = r_0^2 e^{2\ell/\ell_0}, \\ -1, & \tilde{\varepsilon}_Z = \tilde{\mu}_Z = -r_0^2 e^{2\ell/\ell_0} \end{cases} \tag{9.68}$$

in the respective positive and negative quadrants. The conditions of complementarity are satisfied and the dependence along the r axis is irrelevant as

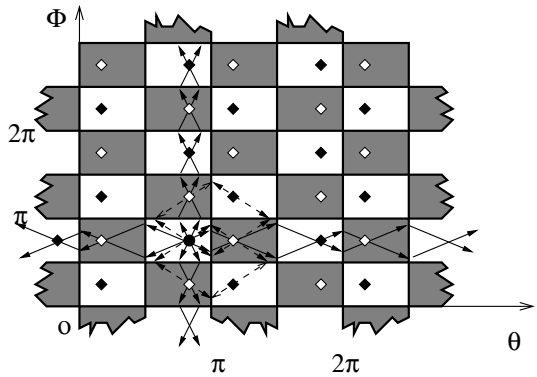

Figure 9.13 A periodic arrangement of cells in checkerboard fashion with adjacent cells having $n = +1$ (white) or $n = -1$ (gray) is shown schematically. If a source is placed in one of the cells, an image forms in every other cell. The properties of the checkerboard are dominated by the modes at the corners. A ray picture only predicts a few of the images as shown.

it is orthogonal (transverse) to the imaging axis along ϕ. Hence we conclude that the images in both the cases of the homogeneous single corner (a) and the homogeneous double corner (b) are perfect and the imaging involves both the propagating and near-field evanescent modes of radiation.

Note that case (b) is unusually singular as the source and the image are imaged onto each other and the fields grow indefinitely in time. It has also been shown that all the surface modes of this system are degenerate at the surface plasmon frequency and the density of modes in the system at this frequency should be infinite (Pendry and Ramakrishna 2003). This mapping into periodic layered media can easily be extended to show that several identical intersecting wedges would also have interesting focusing properties and can image a source onto itself (Guenneau et al. 2005a). It has been shown in He et al. (2005) that there are modes that are essentially trapped at the corners and do not propagate away from them. Thus, the touching corners actually behave like open resonators and can be used to localize light for some time.

9.3.5 Checkerboards and a three-dimensional corner lens

We finally briefly examine an even more singular super-structure of negative refractive index materials obtained by putting together the touching double corners onto a lattice. Rectangular checkerboards of alternating regions of positive and negative refractive index as shown in Fig. 9.13 have been shown to have several interesting electromagnetic properties (Guenneau et al. 2005b). Let us call the axes along the checkerboard directions $\hat{\theta}$ and $\hat{\phi}$, and the direc-

tion normal to the plane as ℓ which is a direction of invariance. Consider that the system is periodic with a period of π along both the $\hat{\theta}$ and $\hat{\phi}$ directions.

Let us define a checkerboard of homogeneous regions with $\varepsilon = \mu = +1$ and $\varepsilon = \mu = -1$ in alternating periodic regions of the checkerboard as shown in the figure. A ray analysis shows that the rays from a source at (θ_1, ϕ_1) can either be trapped around corners or can flow out to the infinities in the crystal while undergoing negative refraction at every interface. The ray analysis obtains a series of images that are formed periodically along the two lines $\theta = \theta_1$ and $\phi = \phi_1$. This decomposition, however, would not be complete for waves for which the interactions with the singular corner points would also be very important. Using the generalized lens theorem, it can be deduced that an image should be formed in each cell of the checkerboard lattice. To show this, let us consider the imaging along, say, the $\hat{\theta}$ direction and use the generalized lens theorem, whereby the condition of complementarity is satisfied for the layers along the imaging $\hat{\theta}$ direction with varying refractive index n in the $\hat{\phi}$ direction transverse to the imaging direction. For a source at $\theta = \theta_1$, $\phi = \phi_1$ in the first positive cell, we have a set of images along the $\phi = \phi_1$ line at $\theta = \pm m\pi \pm \theta_1$ and $-\theta_1$ where m is a positive integer. Similarly, applying the generalized lens theorem along the $\hat{\phi}$ direction, we can show that the entire set of image points would be reproduced along the $\hat{\phi}$ direction. Hence we have an image point in every cell of the checkerboard structure corresponding to the source placed in any one cell. The contradictions that can arise between the ray analysis and a full wave prediction have already been pointed out in Section 9.2.2 and we have one more such case here where the ray analysis reveals only part of the real field distribution.

The presence of a very large number of corners with a high density of modes renders the system very singular. Each corner can support an infinite density of degenerate surface plasmons (Guenneau et al. 2005a). In principle, all the fields of the source would get coupled into the eigenmodes of the corners and the exponentially large fields at the singular points would completely swamp out the inhomogeneous solutions due to the source. Only absorption prevents the actual divergence of the fields in an infinite lattice. On the other hand, a finite checkerboard would imply that all modes (however highly evanescent) in the system are leaky modes and in time escape out of the checkerboard. Numerical studies of checkerboard structures have indeed confirmed this behavior both with respect to the total size of the checkerboard superstructure and with respect to the levels of absorption in the system (Ramakrishna et al. 2007b). Dissipation or finite size regularizes any such unphysical divergence, in which case it becomes meaningful to talk about the properties of checkerboards.

The properties of an extended two-dimensional checkerboard, however, can be utilized to make an important deduction, i.e., the eight touching three-dimensional corners (octants in three dimensions) of negative refractive index can focus light in a similar manner as two-dimensional intersecting corners

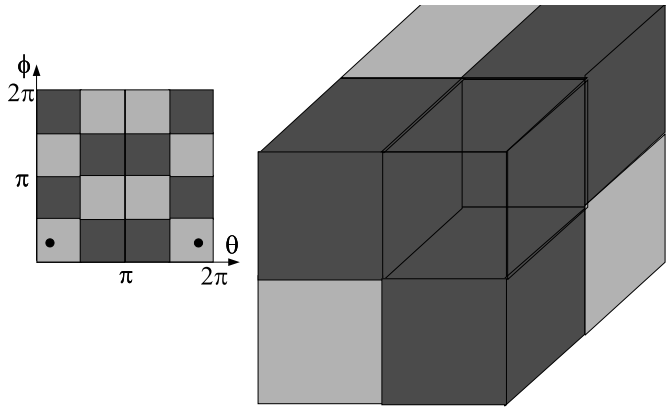

Figure 9.14 The unit cell of the checkerboard on the left with the double periodic set of sources can be mapped into the set of eight alternating three-dimensional corners with alternating positive and negative refractive index ($n = \pm 1$). The corners extend out to the infinities and together act as a three-dimensional open resonator for light.

(quadrants). To show this, consider a checkerboard with the properties

$$\varepsilon_{\pm\theta}(\theta,\phi) = \pm\varepsilon \ \sin\theta, \qquad \varepsilon_{\pm\phi}(\theta,\phi) = \pm\frac{\varepsilon}{\sin\theta}, \tag{9.69a}$$

$$\mu_{\pm\theta}(\theta,\phi) = \pm\mu \ \sin\theta, \qquad \mu_{\pm\phi}(\theta,\phi) = \pm\frac{\mu}{\sin\theta}, \tag{9.69b}$$

where the positive signs and negative signs occur in a checkerboard alternating fashion in space. It is clear that such a system satisfies the conditions of complementarity and mirror anti-symmetry along the main imaging axis ($\hat{\theta}$ or $\hat{\phi}$ in this case), and therefore it should also have imaging properties similar to the homogeneous checkerboards. Also note that the variation of ε and μ along the $\hat{\ell}$ direction is immaterial to the behavior as ℓ is transverse to the imaging axes along $\hat{\theta}$ and $\hat{\phi}$.

Consider making a transformation to spherical polar coordinates from Cartesian coordinates by Eq. (9.40). We obtain the transformation parameters

$$Q_\ell = \frac{r_0}{\ell_0}e^{\ell/\ell_0}, \quad Q_\theta = r_0 e^{\ell/\ell_0}, \quad Q_\phi = r_0 e^{\ell/\ell_0} \ \sin\theta.$$

The renormalized dielectric permittivity $\tilde{\varepsilon}$ and $\tilde{\mu}$ are given by the Eqs. (9.42a) and (9.42b), respectively, and are reproduced below for convenience:

$$\tilde{\varepsilon}_\ell = r_0\ell_0 e^{\ell/\ell_0}\sin\theta \ \varepsilon_\ell, \qquad \tilde{\varepsilon}_\theta = \frac{r_0}{\ell_0}e^{\ell/\ell_0}\sin\theta \ \varepsilon_\theta, \qquad \tilde{\varepsilon}_\phi = \frac{r_0 e^{\ell/\ell_0}}{\ell_0\sin\theta} \ \varepsilon_\phi,$$

$$\tilde{\mu}_\ell = r_0\ell_0 e^{\ell/\ell_0}\sin\theta \ \mu_\ell, \qquad \tilde{\mu}_\theta = \frac{r_0}{\ell_0}e^{\ell/\ell_0}\sin\theta \ \mu_\theta, \qquad \tilde{\mu}_\phi = \frac{r_0 e^{\ell/\ell_0}}{\ell_0\sin\theta} \ \mu_\phi.$$

The variation along the radial $\hat{\ell}$ (transverse) direction is irrelevant and can be ignored. Consider in addition eight three-dimensional corners of homogeneous materials as shown in Fig. 9.14 with alternate wedges having positive or negative refractive index ($n = \pm 1$). Hence we have

$$\varepsilon_\ell = \mu_\ell = \varepsilon_\theta = \mu_\theta = \varepsilon_\phi = \mu_\phi = \pm 1 \tag{9.70}$$

in the corresponding regions. Choosing the scale factor $\ell_0 = 1$, Eq. (9.42a) and Eq. (9.42b) become

$$\tilde{\varepsilon}_\ell = \tilde{\mu}_\ell = \tilde{\varepsilon}_\theta = \tilde{\mu}_\theta = \pm r_0 e^\ell \sin\theta, \quad \tilde{\varepsilon}_\phi = \tilde{\mu}_\phi = \pm \frac{r_0 e^\ell}{\sin\theta}, \tag{9.71}$$

i.e., the system appears just like the two-dimensional checkerboard shown in Fig. 9.14 with spatially varying material parameters considered in the previous paragraph, but with a doubly periodic set of sources with a period 2π along ϕ and θ and a symmetry plane along $\theta = \pi$. Hence, the cubic corner with the homogeneous materials with alternating signs for the refractive index also forms an imaging device with an image point inside every cubic corner. Thus, we have generalized the result of the two-dimensional corner to a three-dimensional corner. An image of the point source in one octant is generated inside all the other seven octants and an image mapped onto the original source point as well. The images are, in a sense, perfect in that both propagating and evanescent waves are involved in the imaging. Thus, a truly three-dimensional open cavity is realized in this configuration. In fact, by considering checkerboards with variations along the $\hat{\theta}$ and $\hat{\phi}$ directions but respecting the condition of a mirror anti-symmetry about the interfaces, one can generate entire classes of interesting configurations of three-dimensional lenses.

We conclude our discussion of checkerboards with an observation on some very interesting properties of triangular (two-dimensional) checkerboards where the cells are equilateral triangles. While a corner of intersection of three finite triangles has some circulating modes about the corner, a ray diagram shows that no ray can escape from a double layer of a triangular checkerboard as shown in Fig. 9.15. This does not, however, hold strictly for a wave, which always has a finite probability of escaping from the finite system. It has been shown that the residence time of waves in the checkerboard can be highly enhanced by layering up the triangles in a concentric manner (Ramakrishna et al. 2007b). The more the number of shells, the better the confinement of radiation. In contrast, this does not hold for a rectangular checkerboard where the ray picture shows that a subset of rays that escapes out of a finite system always exists. Full wave calculations have, indeed, revealed that the residence times in rectangular checkerboards increase comparatively slowly with increase in the number of concentric shells (Ramakrishna et al. 2007b). This confinement holds much potential for enhancing the sensitivity of detectors, or for enhancing non-linearities.

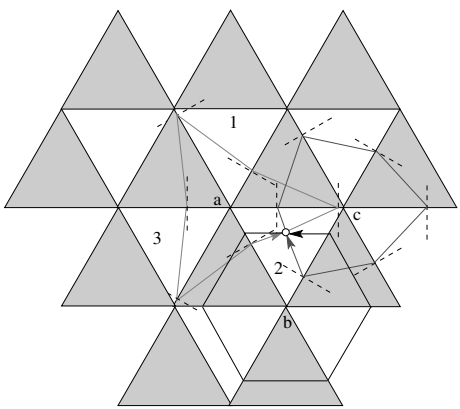

Figure 9.15 Finite checkerboard consisting of alternating regions of positive and negative refractive index media in equilaterial triangular regions. Invariance is assumed normal to the plane of the figure. All rays emitted by a source located in one of the interior triangles are trapped in closed trajectories around one of the three corners.